Exploration of stall dynamics on a high-speed CRM wing

Alessandro Pulimeno

A thesis
submitted in partial fulfillment of the
requirements for the degree of

Master of Science in Aeronautics & Astronautics

University of Washington

2025

Reading Committee:

Owen J. H. Williams, Chair

Antonino Ferrante

Program Authorized to Offer Degree:
Aeronautics and Astronautics

University of Washington

Abstract

Exploration of stall dynamics on a high-speed CRM wing

Alessandro Pulimeno

Chair of the Supervisory Committee:
Owen J. H. Williams
Department of Aeronautics & Astronautics

The sensitivity of the flowfield and the resulting loads/moments are examined on a 4% scale, half-span, high-speed version of the Common Research Model (CRM-HS). A range of Reynolds numbers and angles of attack were examined using a combination of tuft flow-visualization and Particle Image Velocimetry (PIV) in the 8 ft by 12 ft Kirsten Wind Tunnel (KWT) at the University of Washington. The tufts showed a leading edge–tip stall at every tested condition, with separation delayed to higher angles of attack at higher Reynolds numbers (Re). Approximate Reynolds number independence was observed for $Re_c > 10^6$, based on the mean aerodynamic chord. The separation point drifts towards the root for larger angles of attack at the same Re_c condition. PIV data reveal a thickening of the separated shear layer and the formation of reversed flow with consequent vortical structures in the downstream region at a higher angle of attack. We evaluate and compare background subtraction and denoising methods to mitigate low signal-to-noise ratio (SNR) typical of large scale wind tunnels. A POD-based background removal approach proved more robust than average subtraction or high-pass filters, especially in removing model-induced reflections. Conversely, an entropy-based criterion designed to isolate higher order POD modes representing noise, was found to also attenuate turbulent flow features and so it was unsuitable for this dataset. Proper Orthogonal Decomposition (POD) of the top-down PIV data identified a dominant mode pair (modes 1 and 2) exhibiting large-scale spanwise periodicity. These

modes strongly resemble the spanwise alternation seen in stall cells and are phase-shifted to represent a traveling structure in the spanwise direction. The coherent footprint of these modes across the field of view suggests that a low-dimensional mechanism may underlie the separation dynamics. In summary, a highly dynamic reversed flow region and spanwise periodicity are observed which are poorly represented by the mean flow.

TABLE OF CONTENTS

LIST OF FIGURES

NOMENCLATURE

a_j: j^{th} POD coefficient

α: Pitch angle, defined as the angle of attack

AR: Wing aspect ratio, defined as b^2/S_{ref}

b: Wing span

C: Covariance matrix

C_L: Lift coefficient

C_D: Drag coefficient

C_M: Pitching moment coefficient

DC: Direct Current

dt: Time interval

E: Total energy

E_j: Energy of the j^{th} POD mode

λ: Taper ratio

Λ: Sweep angle

MAC: Mean Aerodynamic Chord

$\boldsymbol{\phi}$: POD modes

Re: Reynolds number

Re_c: Chord-based Reynolds number

S_{ref}: Wing reference area

$\mathbf{u}$: Velocity field (vector)

$\mathbf{u}'$: Fluctuating velocity field (vector)

$\mathbf{U}$: Mean velocity field (vector)

$\widetilde{U}$: Reconstructed streamwise velocity

V_c: Convective velocity

X_{ref}: Moment reference center x-coordinate

Y_{ref}: MAC y-coordinate

Z_{ref}: Moment reference center z-coordinate

ACKNOWLEDGMENTS

The support of Boeing Commercial Airplanes, which has funded and endorsed this work. The expertise and guidance of Professor Owen Williams during and beyond the test campaign. Ganesh Bommavaram (MSAA 2024), who co-worked on the design, testing and preliminary data analysis. Ph.D. student Kevin Manohar, for his help to set up the experiment and post-processing. The author would also like to thank the Kirsten Wind Tunnel crew, in particular the Business Manager, Cara Winter, and the Test Engineer, Miguel Salguero.

DEDICATION

Chapter 1

INTRODUCTION

Turbulent flow separation continues to present significant modeling and prediction challenges, preventing confident estimation of the edges of the flight envelope [1]. As a consequence, significant scatter remains in the prediction of maximum wing lift due to the complex, unsteady, and three-dimensional dynamics of separated regions over complex vehicle geometries. The Common Research Model (CRM) serves as a standardized platform for both computational and experimental investigations in this domain. This ecosystem facilitates collaboration among researchers by providing a common geometry, wind tunnel models, and datasets, enhancing the validation and development of computational fluid dynamics (CFD) tools [2, 3, 4]. One of the main challenges to improve CFD modeling is understanding the unsteady separated structure, spanwise variation, and unsteadiness, and its relationship to the mean flow. To close this gap, a full understanding demands that we resolve the time-dependent three-dimensional structures inside the separation zone. Being able to track these coherent vortical motions clarifies how they redistribute momentum and energy and trigger characteristic flow features near the onset of stall along the span. Off-body measurements are therefore essential and often require advanced diagnostic techniques like Particle Image Velocimetry (PIV). These experimental approaches often lead to extremely large datasets that can be compressed with dimensionality-reduction methods such as Proper Orthogonal Decomposition (POD) to isolate the most energetic flow modes [5]. However, techniques such as PIV are not always straightforward to implement in large-scale wind tunnels [6]. Low-speed wind tunnel testing, particularly in large facilities, presents other challenges that make measurements and measurement accuracy even more complex. Related to this aspect is the inherently low signal-to-noise ratio (SNR) prevalent in large, low-speed wind tunnels.

Moreover, larger tunnels require sizable fans, motors, and supporting structures that inherently produce vibrations, adding unwanted mechanical noise to signals [7]. The goal of this work is to provide insight into the complex three-dimensional dynamics of the flow that arise near the onset of stall on a CRM-HS wing, as well as explore ways to improve diagnostic behavior and compensate for noise and low SNR.

Flow separation presents a significant modeling and dynamic challenge, as many conventional turbulence modeling assumptions are violated. Separation often occurs when complex combinations of adverse pressure gradients and surface curvature cause the boundary layer to leave the surface. Both separation and reattachment locations depend on local flow conditions such as Reynolds number, angle of attack, and upstream disturbances [8, 9]. In addition, separation typically exhibits additional distinct features, such as highly unstable shear layers prone to vortex shedding instabilities, periodic low-frequency oscillations, and large changes in separation size due to growth, bursting, and reformation of reversed flow regions [10]. Very low-frequency oscillations are often present, potentially leading to significant variations in aerodynamic forces. This variability results in an inherently unsteady and highly anisotropic flow structure, further complicated by interactions across multiple time and length scales [8, 9, 10].

Recent studies have revealed that flow separation in near or post-stall conditions often manifests in the form of stall cells [11]. These three-dimensional patterns, an example of changing and sometimes sensitive flow topology, result from spanwise instabilities where localized disturbances in the separated shear layer amplify and self-organize into counter-rotating vortex pairs, characterized by a spanwise periodicity. Their formation is highly sensitive to Reynolds number, angle of attack, and wing aspect ratio. The spanwise size of the cells dynamically varies depending on the interaction between flow separation and global aerodynamic conditions, usually ranging from one to three times the chord length [12, 13]. At lower Reynolds numbers, fewer and narrower stall cells appear, while higher Reynolds numbers produce wider cells with more coherent structures. Dell'Orso and Amitay found experimentally that stall cell formation depends on surpassing a critical Reynolds number,

and the resulting flow pattern could shift between full-span separation, single, and dual stall cells depending on angle of attack and Reynolds number [14].In addition to these geometric characteristics, recent studies have also revealed important aspects of their dynamics. Plante et al. [12] showed that when sweep is present, stall cells convect steadily in the outboard direction with a speed proportional to the crossflow component of the freestream velocity, scaling approximately as $V_c/U_\infty \approx 0.7\tan(\Lambda)$, where Λ is the sweep angle. This convection introduces a characteristic unsteady frequency linked to the cell spanwise spacing and convection speed. Manni et al. [13] numerically confirmed that the formation of stall cells is closely tied to the slope of the lift curve in the post-stall regime: stall cells emerge when the slope of the lift curve becomes negative, and their spanwise spacing can be predicted from the slope. Detecting stall cells in mean flow measurements poses significant challenges due to their inherently unsteady and sensitive nature. Stall cells often coexist with strong turbulent fluctuations and spanwise variations, causing their time-averaged footprint to be weak or ambiguous. Although mean stall cells are not always evident in time-averaged fields, unsteady spanwise periodicity of separated regions is well known. This study explores the potential similarities between these unsteady structures and stall cells in a configuration with more complexity than the conventionally studied rectangular wing with constant cross-section.

Previous studies on bump geometries, chosen to have relevance to high-lift configurations, identified instantaneous vortex structures resulting from interactions between spanwise and streamwise motions of the recirculation zone, characterized by alternating pairs of vortices across the span. These patterns originate from low-frequency oscillations and spanwise instabilities of the separated flow, which yield to the so-called "breathing motion", creating a recognizable symmetrical vortex topology ("owl-face") in the instantaneous flow fields [15, 16]. Similarly, stall cells observed on wings result from spanwise instabilities in the separated shear layer, forming periodic counter-rotating vortex pairs. In both cases, the fundamental mechanism is an instability in the separated shear layer that leads to organized, three-dimensional coherent structures, each with characteristic spanwise periodicity.

This work aims to address the following questions: How sensitive is the flow to variations

in Reynolds number and angle of attack? Which flow features are present in the mean or unsteady modes? How can we deal with low SNR and, in general, hardware limitation when testing in large scale facilities? How much does the instantaneous flow deviate from the commonly studied mean flow picture?

Chapter 2
APPARATUS AND METHODS

2.1 Model and Facility

The test model was a 4%-scale half-model CRM-HS without vertical-tail, nacelle, or pylon components. The wing planar view is given in Fig. 2.1, and its reference full-scale geometric quantities are listed in Table 2.1 with respect to the conventional CRM global reference system [4]. The fuselage edge is at 10% of the semispan, and the trailing edge kink is at the 37% station.

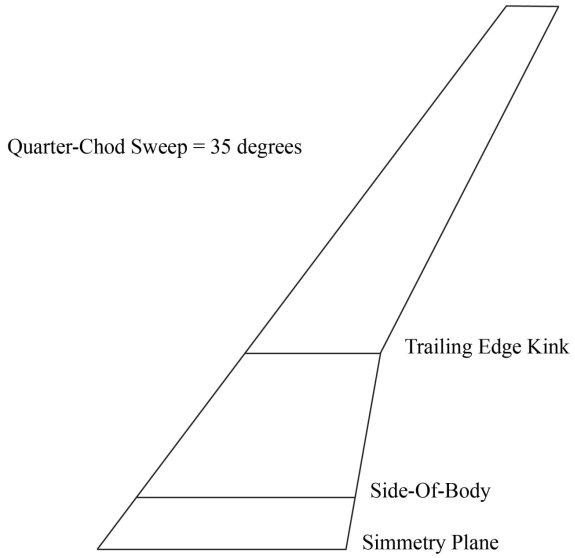

Figure 2.1: Planar view of the CRM wing geometry

Table 2.1: Reference Quantities for full scale CRM [17] (units converted to SI).

Quantity	**Value**
Sref/2	191.792 m^2
MAC	7.006 m
Semispan (b/2)	29.384 m
Xref	33.682 m
Yref	11.906 m
Zref	4.520 m
λ	0.275
$\Lambda_{C/4}$	35°
AR	9.0

All experiments took place in the subsonic Kirsten Wind Tunnel (KWT) at the University of Washington. This is a double-return, closed-circuit wind tunnel with a rectangular test

section measuring 8 ft high, 12 ft wide, and 10 ft long; the test section corners have 45° chamfers. Two propellers powered by 500-horsepower DC motors provide a velocity range of 2–90 m/s, enabling dynamic pressures up to 100 psf [18]. The chord-based Reynolds number range for this 4% model is

$$3.8 \times 10^4 < Re_c = \frac{U_\infty c}{\nu} < 1.67 \times 10^6,$$

where U_∞ is the free-stream velocity, c is the MAC, and ν is the kinematic viscosity of air. The freestream turbulence intensity is approximately 0.72% of U_∞ and currently under re-assessment [18]. The model was mounted on a 6-degree-of-freedom external side-wall balance (SWB) on side of the test section, with $\alpha = 0°$ set according to the model waterline reference [4]. Pitching up yields positive angles of attack. A rendering of the CRM-HS model in the KWT test section is shown in Fig. 2.2.

A potential source of uncertainty in any half-model test is the wall boundary layer (BL) that builds up ahead of the mounting wall. In the present campaign, this boundary layer thickness was not measured directly, and no splitter plate or BL control was used. One attempt to acount for this boundary layer was a constant-thickness peniche between the model centre-plane and the tunnel wall [19]. Because the boundary layer state remains uncertain, the absolute values of measured forces and moments should be regarded as indicative of overall trends, rather than as definitive full-span equivalents.

2.2 Forces/Moments Measurement

Loads corresponding to lift (L), drag (D), and pitching moment ($C_{M_{0.25c}}$) were acquired via the 6-degree-of-freedom external SWB. Data were sampled at 1 kHz and averaged over approximately 35 s. Prior to each wind-on test, a wind-off zero (WOZ) was recorded to account for the model's center of gravity (CG) effects. Any balance shifts due to CG variations during rotation at $q = 0$ psf were captured in the WOZ condition and used for weight tare corrections. No other corrections, such as blockage, wall, or flow angularity, were applied to the data. The aerodynamic moments, initially referenced to the Balance Moment Center

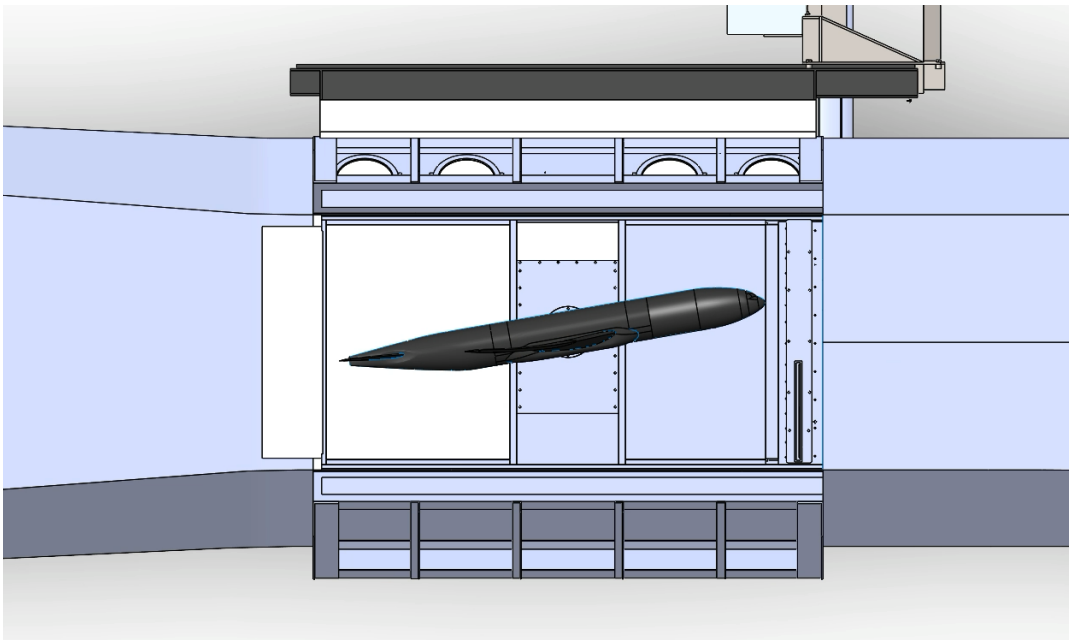

Figure 2.2: Rendering of the 4%-scale CRM-HS model mounted to the KWT side wall balance.

Table 2.2: KWT Sidewall Balance full-scale (F.S.) limitations and uncertainties for Lift, Drag, and Pitching Moment.

Term	**Full-Scale Magnitude**	**Typical Uncertainty**	**Max. Uncertainty**	**Typical Rel. Uncertainty**	**Max. Rel. Uncertainty**
Lift	3314.4 N	±3.324 N	±13.097 N	±0.1003% F.S.	±0.3953% F.S.
Drag	978.6 N	±1.970 N	±4.911 N	±0.2013% F.S.	±0.5016% F.S.
Pitch Moment	1339.3 Nm	±1.482 Nm	±20.606 Nm	±0.1106% F.S.	±0.3465% F.S.

(coinciding with the trunnion), were shifted to the model quarter-chord MAC using

$$M = M_{\text{bal}} + L \cdot x_{\text{off}} \quad , \tag{2.1}$$

where $x_{\text{off}} = -0.12\,\text{m}$. Table 2.2 summarizes the balance force and moment limits and uncertainties.

The aerodynamic coefficients were non-dimensionalized using the reference quantities from Table 2.1, scaled to 4%, and the expressions

$$C_L = \frac{L}{q_\infty S_{ref}} \quad , \qquad C_D = \frac{D}{q_\infty S_{ref}} \quad , \qquad C_M = \frac{C_{M_{0.25c}}}{q_\infty S_{ref} c} \quad . \tag{2.2}$$

Data were acquired during flow-visualization tests over a range of angles of attack (–3° to 19.5° in 1.5° increments, both upsweep and downsweep) at three dynamic pressure conditions corresponding to different Re_c (Table 2.3).

2.3 Flow-visualization

Tuft flow-visualization was used to explore Reynolds number and angle of attack sensitivity of flow separation over the CRM-HS wing and to help select PIV measurement locations. The model was prepared using 3M 2080 series vinyl wrap following manufacturer instructions. Tufts (from a T41 trilobal fluorescent polyester monofilament, $\approx 0.23\,\text{mm}$) were laid out at

approximately 2.54 cm spanwise spacing and taped in long chordwise strings. Polyurethane glue (thinned with acetone) was applied at 1.27 cm chordwise spacing, then the tufts were separated at the leading edge and trimmed.

Data were collected in from of video recordings acquired using a CanonT6i DSLR camera in Full High Definition (FHD) quality at 30 frame-per-second (fps). The camera was installed on a custom-designed traversing frame, having a top-down view of the model wing. Each test condition (combination of Re_c and angle of attack) was kept steady for at least 34 s in order to collect a minimum of 1000 frames for the post-processing analysis.

Tuft recordings were processed according to the procedure detailed by De Voogt and Ganapathisubramani [20]. First, the images are converted to greyscale. To enhance the contrast of the tufts, consecutive images from the recording are then subtracted. This subtraction is done by shifting the images forward by one time step and calculating the difference between the shifted images and the original, unshifted images at each time step. This process removes most of the static elements in the images over a moderate time scale while retaining the unsteady tufts. Next, 10 subtracted images, sampled linearly across the time frame, were added together. Lastly, tuft motion is color-coded to emphasize different flow regimes. The color green designates a preferred direction, meaning that, on average, the specific tuft spent more time in the green area, while red indicates greater variability. Figure 2.3b and 2.3c shows examples of video recordings that have been processed into single images, whereas Fig. 2.3d shows the final color-coded image.

A summary of the flow-visualization test conditions is provided in Table 2.3.

2.4 Particle Image Velocimetry

Particle Image Velocimetry (PIV) is a non-intrusive, optical measurement technique used to obtain instantaneous spatial velocity fields in fluid flows. In its planar form, PIV measures two velocity components over a two-dimensional plane (2D2C). The method involves seeding the flow with tracer particles that follow the fluid motion, illuminating a thin slice of the flow with a pulsed laser sheet, and recording two consecutive images of the particle distribution.

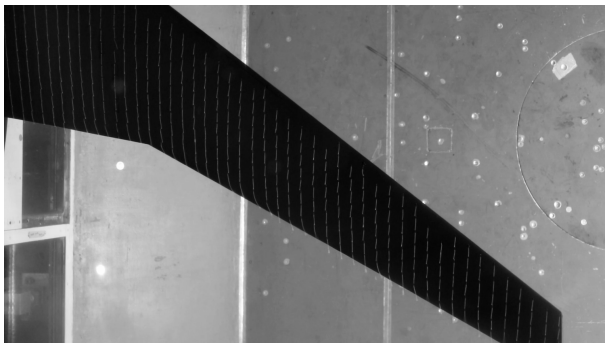

(a)

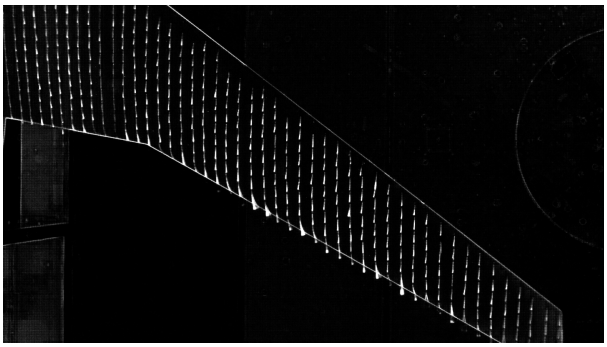

(b)

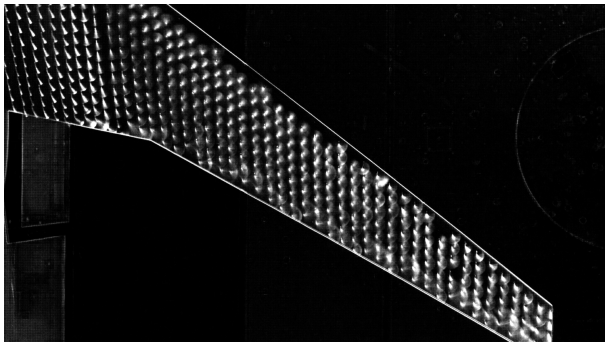

(c)

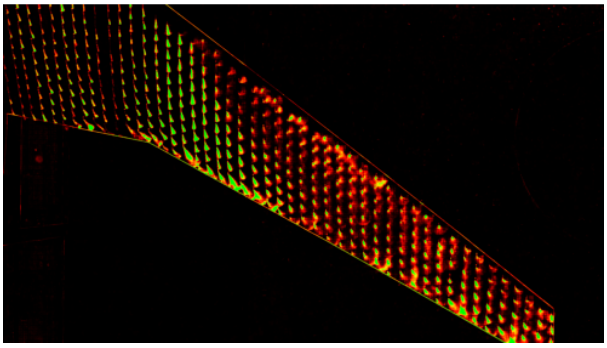

(d)

Figure 2.3: Tuft images at $Re_c = 10^6$: (a) original greyscale frame; (b) processed image for attached flow; (c) processed image for separated flow (starting at approximately 35% of the semispan); (d) final color-coded image where two different flow regimes are visible.

Table 2.3: Flow-visualization test conditions summary.

Run	q_∞ **[psf]**	Re_c	α **range (start:step:stop)** [°]
1	8	0.47×10^6	-3:1.5:19.5 & 19.5:-1.5:-3
2	32	10^6	-3:1.5:19.5 & 19.5:-1.5:-3
3	100	1.67×10^6	-3:1.5:10.5

By analyzing the particle displacements between the two images over a known time delay, the in-plane velocity components are reconstructed [21, 22, 23]. Each PIV image pair is divided into interrogation windows, and the most probable particle displacement within each window is estimated through spatial cross-correlation. The displacement vectors are then divided by the known time interval to obtain velocity vectors. The technique offers spatially-resolved velocity measurements over the illuminated plane without requiring intrusive probes. A detailed overview of the method, including practical guidelines for experimental design and error estimation, is provided in [24].

Two-component, single-camera planar PIV experiments were conducted in two orthogonal planes. One measurement was in a quasi streamwise–vertical ("side-on") plane with the camera canted to align one edge with the wing chord at $\alpha = 12°$, and one in a streamwise–spanwise ("top-down") plane tangent to the wing leading edge. A rendering of both setups is shown in Fig. 2.4.

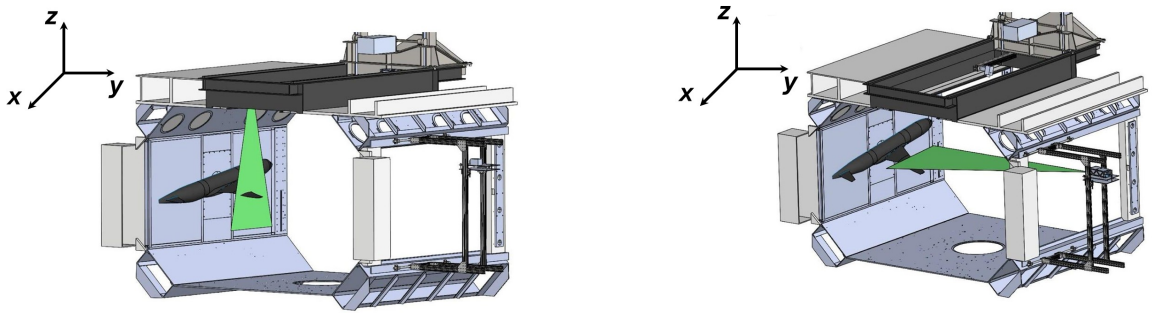

(a) (b)

Figure 2.4: Renderings of the side-on (streamwise–vertical) a and top-down (streamwise–spanwise) b PIV setups. The general KWT axis orientation is shown in the top-left corners.

A Quantel EverGreen 200 dual-pulsed Nd:YAG laser (200 mJ/pulse at 532 nm, 15 Hz) generated a ≈2 mm thick laser sheet to illuminate approximately 1μm DEHS particles seeded

by a LaVision Aerosol generator. Images were captured with a 5.5-megapixel Imager scientific sCMOS camera (2560×2160 pixels). For the side-on configuration, a field-of-view (FoV) of 25.2 cm×21 cm was achieved using a Nikon 300 mm lens at $f/12$. For the top-down configuration, a FoV of 38.7 cm×32.8 cm was captured with a Nikon 60 mm lens at $f/8$. After calibration, scaling factors were determined as 10.12 pixels/mm for side-on and 6.6 pixels/mm for top-down. Table 2.4 summarizes the PIV configurations and conditions. Interframe times were chosen so that maximum particle displacements were approximately 16 pixels; considering a typical peak fit uncertainty of 0.1 pixels [23], the resulting random velocity error is about 0.6% which translates in less than 0.4 mm s^{-1}.

Table 2.4: Summary table of PIV test conditions. "Samples" indicates the number of snapshots acquired for each configuration; "dt" is the inter-pulse time.

Configurations	q_∞ **[psf]**	Re_c	α [deg]	**Samples**	**dt** [μs]
Side-on PIV	8	0.47×10^6	12	1500	47
	32	10^6	10.5, 12, 13.5	3000	24
	70	1.48×10^6	12	1500	16
Top-down PIV	8	0.47×10^6	12	1500	80
	32	10^6	12	3000	40

Image acquisition, calibration, and initial post-processing were controlled via LaVision DaVis 10.2 software. Images were stabilized to counteract vibrations. For side-on, an average subtraction time filter (length = 45 images) was used to remove the steady background, and for the top-down configuration a Butterworth high-pass filter (length = 45 images) was applied. Hand-drawn masking excluded regions of high reflectance. Multi-pass cross-correlation analysis was performed using a first pass with 256 × 256 pixel windows (50% overlap) and subsequent passes with 32×32 pixel windows (75% overlap). Outlier detection was applied using a Universal Outlier filter (11×11 window, threshold 1.5) [25]. The resulting

vector fields were exported for further statistical and modal analysis.

2.5 PIV Data Post-processing and Coordinate Systems

The processed PIV data were imported into Python and Matlab for analysis. The wind tunnel's global coordinate system is shown in Fig. 2.4: x is streamwise (parallel to the flow), y is spanwise (perpendicular to the side wall), and z is vertical (perpendicular to the floor).

Data are presented in different coordinate systems depending on the PIV configuration and alignment of the camera with the wing chord. For the side-on orientation, data were acquired so that the camera frame edge aligned with an angle of 12°. Results are presented in a coordinate system (x_c, z_c) with x_c aligned with $U_\infty \cos(12°)$ and the origin set at the wing's leading edge at the measurement location. Velocities (mean and fluctuations) are defined as $u_c = U_c + u'_c$ and $w_c = W_c + w'_c$ in the x_c and z_c directions respectively.

For the top-down view, an additional rotation of $-35°$ about the z-axis was applied to align with the wing's leading edge (with 35° being the sweep angle as given in Table 2.1). Results are presented in coordinates (x_{LE}, y_{LE}) with the edge of the FOV set upstream of the leading edge at $x_{LE}/c = -0.2$. Velocities are defined as $u_{LE} = U_{LE} + u'_{LE}$ and $v_{LE} = V_{LE} + v'_{LE}$. Due to the wing's camber and dihedral, the vertical distance from the wing surface varies with both the chord-wise and spanwise directions; at $x/c \approx 0.25$, the offset is approximately 5 mm.

2.5.1 Calculation of POD modes

To investigate the most energetic flowfield modes and explore their temporal variation, the Proper Orthogonal Decomposition (POD) was employed [5, 26]. This method decomposes the velocity fluctuations into spatial modes and their corresponding temporal coefficients, resulting in the following approximation of the velocity field:

$$\mathbf{u}(\mathbf{x}, t) \approx \mathbf{U}(\mathbf{x}) + \sum_{j=1}^{N} a_j(t)\boldsymbol{\phi}_j(\mathbf{x}) \quad , \tag{2.3}$$

such that the fluctuating component $\mathbf{u}'(\mathbf{x},t)$ is approximated as $\mathbf{u}'(\mathbf{x},t) \approx \sum_{j=1}^{N} a_j(t)\boldsymbol{\phi}_j(\mathbf{x})$ [27]. Here, $\boldsymbol{\phi}_j(\mathbf{x})$ represents the spatial mode shapes, and $a_j(t)$ are the temporal coefficients. Snapshot POD utilizes a series of uncorrelated flow realizations upon which the two-point covariance matrix is constructed as:

$$\mathbf{C}\left(\mathbf{x},\mathbf{x}'\right) = \frac{1}{N}\sum_{n=1}^{N} \mathbf{u}'^{\top}\left(\mathbf{x},t^n\right)\mathbf{u}'\left(\mathbf{x}',t^n\right) \quad , \tag{2.4}$$

where N is the number of snapshots given in Table 2.4. The associated eigenvalue problem can then be formulated as $\mathbf{C}\ \mathbf{A} = \lambda\mathbf{A}$. Solving this problem results in a complete set of N orthogonal eigenvectors $\{A_i, i = 1,\ldots,N\}$. Both eigenvectors and eigenvalues are ordered in decreasing order ($\lambda_1 > \lambda_2 > \ldots > \lambda_M$). The eigenvalues are directly related to the energetic content of the corresponding mode via $E_j = \lambda_j/E$, where E is the total energy given by the sum of all the eigenvalues [28]. The elements of these eigenvectors are then used in the construction of the POD modes

$$\boldsymbol{\phi}_i(\mathbf{x}) = \frac{\sum_{n=1}^{N} A_i^n \mathbf{u}'(\mathbf{x},t^n)}{||\sum_{n=1}^{N} A_i^n \mathbf{u}'(\mathbf{x},t^n)||}, \quad i = 1,\ldots,N. \tag{2.5}$$

The expansion coefficients are determined by projecting the velocity field onto the POD space

$$\mathbf{a} = \boldsymbol{\Phi}^{\top}\mathbf{u}', \tag{2.6}$$

where $\boldsymbol{\Phi} = [\boldsymbol{\phi}_1\ \boldsymbol{\phi}_2\ \cdots\ \boldsymbol{\phi}_N]$ and $\mathbf{a} = [\boldsymbol{a}_1\ \boldsymbol{a}_2\ \cdots\ \boldsymbol{a}_N]$.

2.6 Noise reduction techinques

When performing PIV, especially in large scale facilities, there are different factors that can undermine the overall quality of the data. Among the other, the low SNR when big distances are involved and considerable reflection areas caused by the model itself and wind tunnel walls. Although the LaVision DaVis software does a decent job in mitigating these effects, several attempts were made to further improve data quality. The approaches presented here are based on POD and aim to further reduce wall reflections, as well as trying to identify a

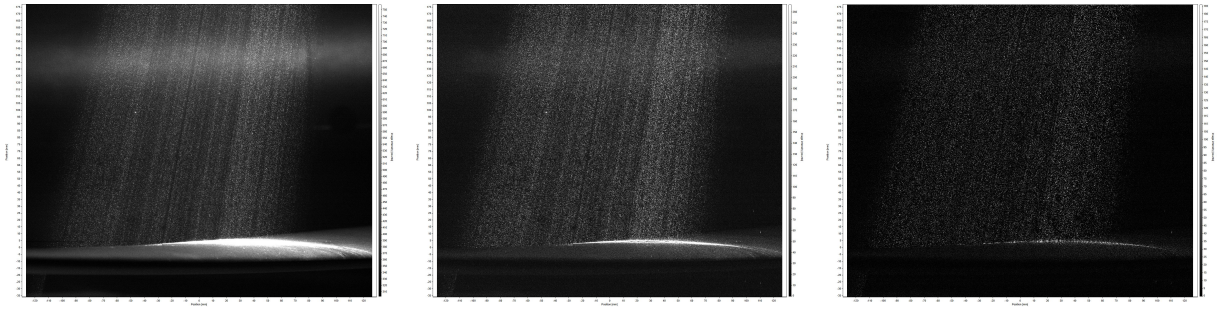

(a) (b) (c)

Figure 2.5: Raw PIV images as acquired by the sCMOS camera (a); PIV image processed with average subtraction filter (b); PIV image processed with POD background subtraction method (c).

threshold at which POD modes predominantly represent noise rather than coherent dynamics of the flow. The hope is that removing these modes, will lead to mitigate regions retained to be non-physical when evaluating mean fields and flow statistics.

2.6.1 POD-based background subtraction

Upon the image stabilization step, the applied techniques were not able to completely remove the reflections from the model and the wind tunnel floor (in the background of the top-down configuration), therefore the method from Mendez and collaborators was used to further mitigate these undesirable features [29]. The approach applies a Proper Orthogonal Decomposition (POD) to the sequence of raw PIV images, exploiting the fact that background reflections tend to be more spatially and temporally coherent than the motion of tracer particles. By identifying and removing the dominant POD modes associated with the static or slowly varying background, a filtered image sequence is reconstructed that preserves the particle pattern while significantly attenuating unwanted reflections. A comparison of the background removed PIV images is given in Fig. 2.5.

Two clear large reflection zones can be observed in Fig. 2.5a: one in the upper part of the image, caused by the wind tunnel wall; one of the wing itself, caused by the laser impinging on the wing. It can be noted that the subtraction filter is able to reduce the intensity of both reflections, without affecting the particles significantly, however, small "shadows" are still present in the upper part of Fig. 2.5b and the reflection of the wing still covers most of the near-wall region. In Fig. 2.5c, on the other hand, the wind tunnel wall reflection has been significantly reduced, the wing reflection is very shallow compared to Fig. 2.5a-b, and the particles are preserved. The POD method is robust against variations in background intensity and gradient, and it operates efficiently even when the sequence is not time-resolved, as in this case. Here, we present a comparison of the streamwise Reynold stress for the top-down configuration computed using datasets originating from the two different background subtraction pipelines.

2.6.2 Entropy line fit method for automatic mode selection for ROM

When evaluating mean field and flow statistics, we found different regions of peak or minimum stresses retained to be not physical. In particular, in Fig. 2.7a, it is evident how one region of peak stress is present in the mid span region of the leading edge and one region of minimum stress is observed toward the root of the FOV.

Proper Orthogonal Decomposition (POD) was introduced to obtain spatial modes $\phi_j(\mathbf{x})$ and temporal coefficients $a_j(t)$ for the measured velocity fields. While retaining all N modes would reproduce the data exactly, it would also re-introduce measurement noise, and other artifacts. Conversely, an arbitrary truncation risks eliminating energetically modest but dynamically important structures. An objective, data-driven criterion is therefore required to identify the smallest subset of modes that captures the coherent flow content while suppressing noise. The mode-selection strategy adopted here follows the entropy–line–fit (ELF) method [30]. For every POD mode j we compute the two-dimensional discrete-cosine transform (DCT) of the mode and evaluate its Shannon entropy [31, 32]

$$S_j = -\sum_k p_{j,k} \log_2 p_{j,k}; \qquad p_{j,k} = \frac{|c_{j,k}|}{\sum_m |c_{j,m}|}, \tag{2.7}$$

where $c_{j,k}$ is the k-th DCT coefficient of mode j. Coherent structures compact into a small number of large-magnitude DCT coefficients and thus exhibit low entropy; noise-dominated modes approach the theoretical maximum entropy values, building a plateau. Therefore, plotting S_j versus mode index j produces an initially rising curve that plateaus once the spatial spectrum becomes indistinguishable from white noise. The plateau onset ($j = j^*$) is automatically detected via the two-line fit method. For every candidate split index, one straight line if fit to the entropy values before the split and another to those after the split. For each segment the R^2 value is computed and averages, the a fitting error Σ, defined here as the sum of squared residuals between the measured and fitted entropies is also calculated; this procedure is iterated for all points in the signal. The best fit will minimize the error and maximize the average R^2 value of the two lines. Thus, the optimal cutoff is selected as the point, where R^2/Σ, is maximized. An example of how this iterative method is implemented is given in Fig.2.6a.

The value of the selection criterion (R^2/Σ) for the top-down nominal case ($Re_c = 10^6$, $\alpha = 12°$) is shown in Figure 2.6.

Figure 2.6b shows one clear peak where the R^2 value normalized by the fitting error, reaches its maximum. The peak corresponds to 257 POD modes, meaning that adding other modes to the reconstruction will most likely only reintroduce measurement noise. For the $Re_c = 0.67 \times 10^6$ case, where only 1500 snapshots were recorded, the optimal number of modes is found to be 88.

In the following, we present a comparison of the streamwise Reynold stress for the top-down configuration computed using the raw vector field data (i.e. full rank reconstruction), applying POD background subtraction only, and the ROM given by the ELF criteria.

In Fig. 2.7b, the POD filter is able to somewhat mitigate the peak stress caused by reflection, however, the region of minimum stress in the mid-span root portion of the wing, likely

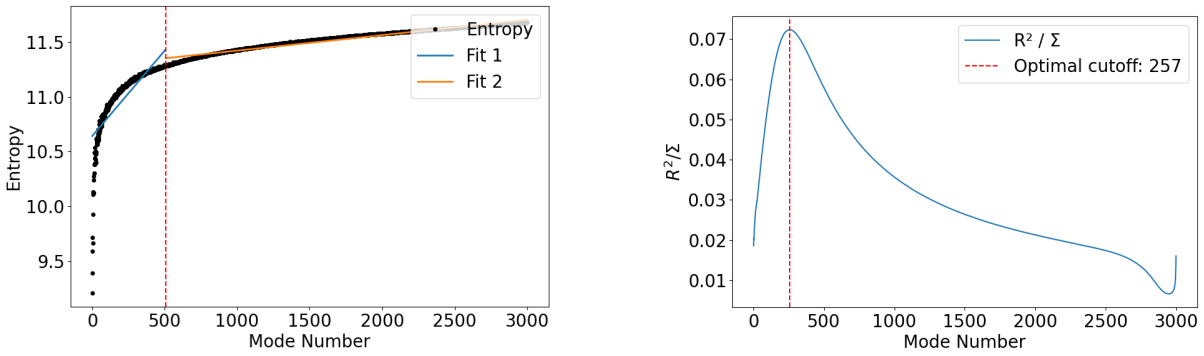

(a) (b)

Figure 2.6: Entropy line fit method (a). Cutoff number of modes identified via the ELF method (b).

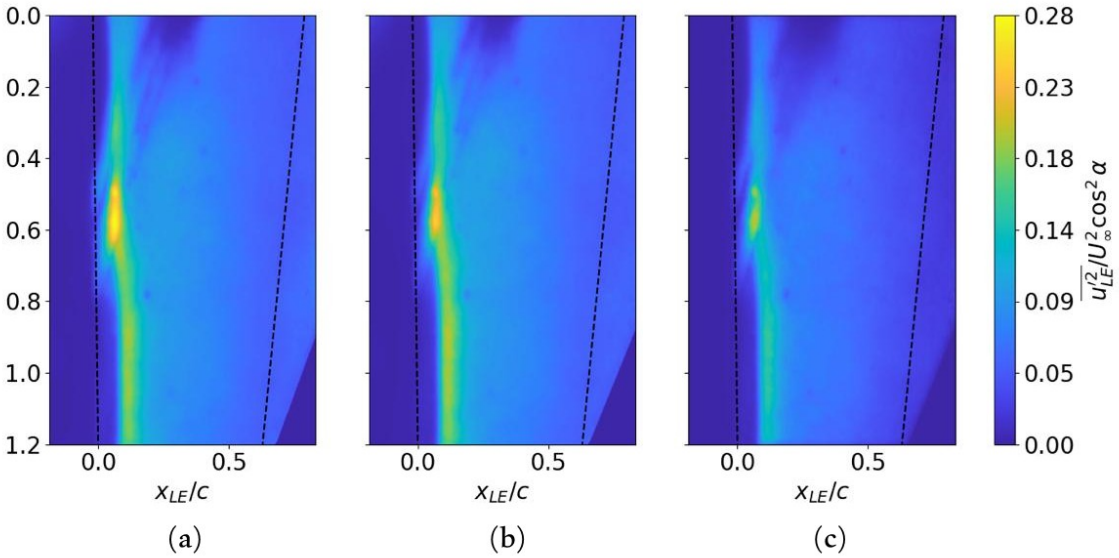

(a) (b) (c)

Figure 2.7: Streamwise Reynold stress calculated with raw data (a); with Butterworth high-pass filter (b); with ELF reconstruction (c).

caused by a model shadow, is still only partially improved. On the other end, background images and wall reflections are still present for some sensitive metrics. Effectiveness of this subtraction method would likely be increased by improvements to the image signal-to-noise ratio, which is stretched by the large domains being measured in this large tunnel. The POD-background subtraction method led to an improvement, in terms of "bad vectors", of 8% when compared to the raw processed data.

When evaluating the ROM reconstruction (Fig.2.7c), we can observe how the peak stress is attenuated, further justifying that the region is dominated by noise (i.e. laser reflection in this case). Moreover, the region of minimum stress in the mid-span root portion of the wing, results more homogeneous when compared to Fig. 2.7a and b. It is important to point out that, although the method seems to be effective in mitigating reflection areas, it was found to attenuate physical peak region on the leading edge.

Chapter 3

RESULTS

We explore the sensitivity of the forces/moments and flowfields over the CRM-HS wing, focusing on the influences of angle of attack and Reynolds number. Refer to §2 and Table 2.3 for the range of conditions explored in this study. Loads and moments are elaborated in §3.1 and the result of tufting visualizations is described in §3.2. These tufting results were then used to narrow test conditions for further PIV analysis. Flowfield mean flow behavior and flowfield statistics are illustrated in §3.3.1 and 3.3.2, lastly insights arising from an exploration of the most energetic POD modes are discussed in §3.4.

3.1 Model loading

CRM-HS forces and moments coefficients are shown in Fig. 3.1(a,b,c), covering a range angles of attack and for three Reynolds numbers. Results are shown for a positive pitch rate (upsweep) only. Data were not acquired at the highest angle of attack for the highest Reynolds number as the tunnel was shut down mid-run as some of the tufting detached from the model.

The lift coefficient shows a linear trend until 7.5° for $Re_c = 0.47 \times 10^6$ and until 9° for larger Reynolds numbers. The lift curve slope of the linear segments is similar across all Re, it being approximately $6.6\,\mathrm{rad}^{-1}$. Maximum lift was not achieved within the range of angles of attack tested, as is sometimes observed for this type of model. The drag coefficient is relatively insensitive to α at low angles of attack, and less than 0.09. It starts to rise sharply at 7.5° for $Re_c = 0.47 \times 10^6$ and at 9° for higher Re, reflecting the behavior observed for the lift coefficient, where it deviates from the linear trend observed at small angles of attack.

The pitching moment starts at approximately $C_M \approx 0.35$ at $\alpha = -3°$, and decreases

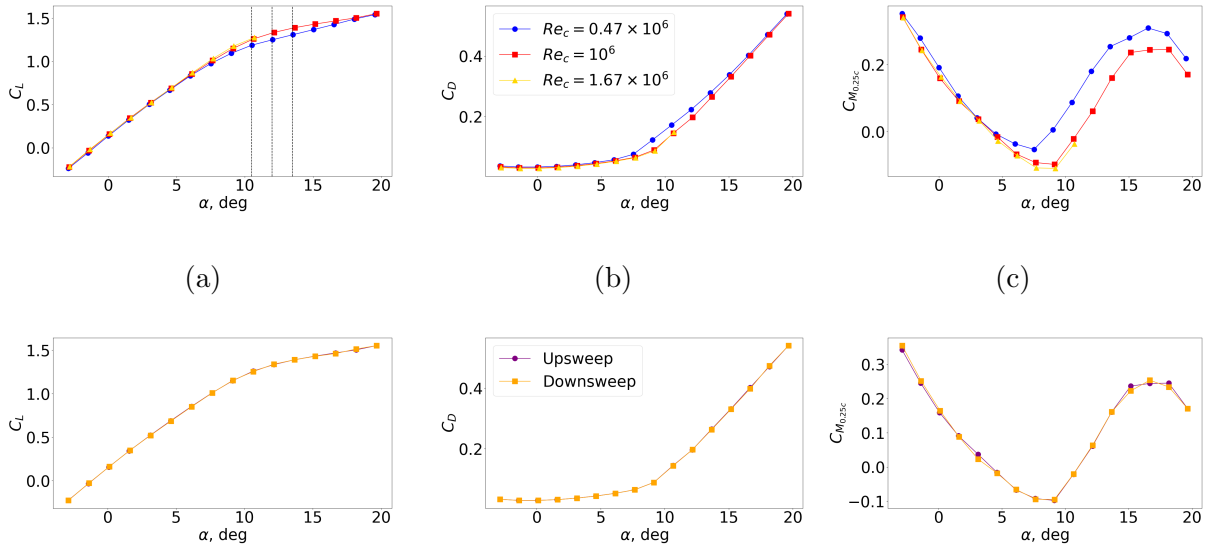

Figure 3.1: Aerodynamic performance of CRM-HS wing across Reynolds number range (a-c) for a pitch up direction only (upsweep); vertical dashed line at $\alpha = 10.5°$, 12°, and 13.5°. (d-f) Difference between upsweep and downsweep results for $Re_c = 10^6$.

approximately linearly until 6° for $Re_c = 0.47 \times 10^6$ and until 7.5° for larger Reynolds numbers. The slope of those linear segments is similar for all three Re, it being approximately $-2.45\,\mathrm{rad}^{-1}$. The pitching moment minima are achieved at 7.5° and 9° for $Re_c = 0.47 \times 10^6$ and $Re_c \geq 10^6$ respectively. C_M is negative for $4.5° \leq \alpha \leq 9°$ for low Re, whereas it stays negative till 10.5° for the two higher Re cases. This behavior is characteristic of flow conditions where the aerodynamic center of the model generates a restoring (nose down) pitching moment as C_L increases with the angle of attack. Furthermore it suggests differences in the structure of the separation is different at lower angles of attack for the lower Re. The pitching moment results are observed to be overall more sensitive to both Reynolds number and angle of attack than the lift and drag. This would be consistent with greater sensitivity to small changes in flow separation since this would induce shifts in the center of pressure location that influence the lift and drag coefficients less.

After reaching its minima, C_M start rising following a linear trend up to 13.5° for $Re_c = 0.47 \times 10^6$, and up to 15° for the higher Reynolds numbers. The slope of the two lines are once again similar, however they are shifted by $C_{M_{0.25c}} \approx 0.1$ at a given angle of attack, where larger values are recorded for small Re. The secondary maximum appears when moment stall is achieved, at 16.5° for the lower Re and at $\alpha = 18°$ for $Re_c = 10^6$. In general, the magnitude of the pitching moment is slightly larger at lower Re.

As flow separation can sometimes exhibit hysteresis effects, data were acquired on both the upsweep and downsweep. Figure 3.1(d,e,f) reveals differences between each pitching direction for the middle Reynolds number of $Re_c = 10^6$. Both lift and drag coefficients show no significant differences in the upsweep and downsweep data. In contrast, the pitching moment coefficient (Fig. 3.1f) reveals some deviations for α between 14° and 18°, close the the local maximum. Exploration of these results for all Reynolds numbers reveal that the local maximum is achieved at a slightly lower angle of attack for the downsweep data in all cases. The source of these these discrepancies is unknown, however, may be attributed to hysteresis dynamics in the separation-reattachment process or the presence of slow, large-scale separated structures that require long time-averaging to achieve a converged sample.

Time series of loading and moment data will be explored in more detail in future studies to help isolate the source of this variation but were not saved for the current study.

These measurements suggest that changes to the separated structure, location and topology are likely to be occurring between $10 \leq \alpha \leq 16$ with visualizations and PIV required to further confirm this hypothesis.

3.2 Tuft visualizations

Tufted flow visualization videos were recorder for the full pitch up and pitch down loads/ moments measurements, aiming to provide insights into Reynolds number and angle of attack sensitivities. Figure 3.2, highlights a series post-processed images at different angles of attack for which the greatest variation was observed between each 1.5° angle of attack step. Only the lowest and middle Reynolds numbers are highlighted as the difference between the middle and highest Reynolds numbers was minimal. A complete set of images can be found in Appendix A, where we show the pitch up and pitch down data for angles between 6° and 18° ($Re_c = 10^6$).

Broadly, the CRM-HS wing produced a leading edge/tip stall that was observed to be consistent across the full dataset. Separate flow, interpreted as more variation in the motion of the tuft (redder color), was first observed at $\alpha = 7.5°$ for $Re_c = 0.47 \times 10^6$ and $\alpha = 9°$ for $Re_c \geq 10^6$. This angle of attack aligns with those at which the lift and drag coefficients showed changes in behavior and the pitching moment coefficient reached its minimum in §3.1.

It is observed that the separation line, defined as the region between separated flow (tufts random motion, prevalently in red) and attached flow (prevalently in green) moves towards the root with increasing angle of attack. This progression in flow behavior is consistently evident across all Reynolds numbers tested. For higher Re, the separation is delayed compared to lower Re. For instance, as shown in Figs. 3.2a, 3.2c, and 3.2e, separated flow covers the entire wing past the trailing edge kink at all angles of attack for $Re_c = 0.47 \times 10^6$. Conversely, Figs. 3.2b, 3.2d, and 3.2f for $Re_c = 10^6$ exhibit a region of attached flow between

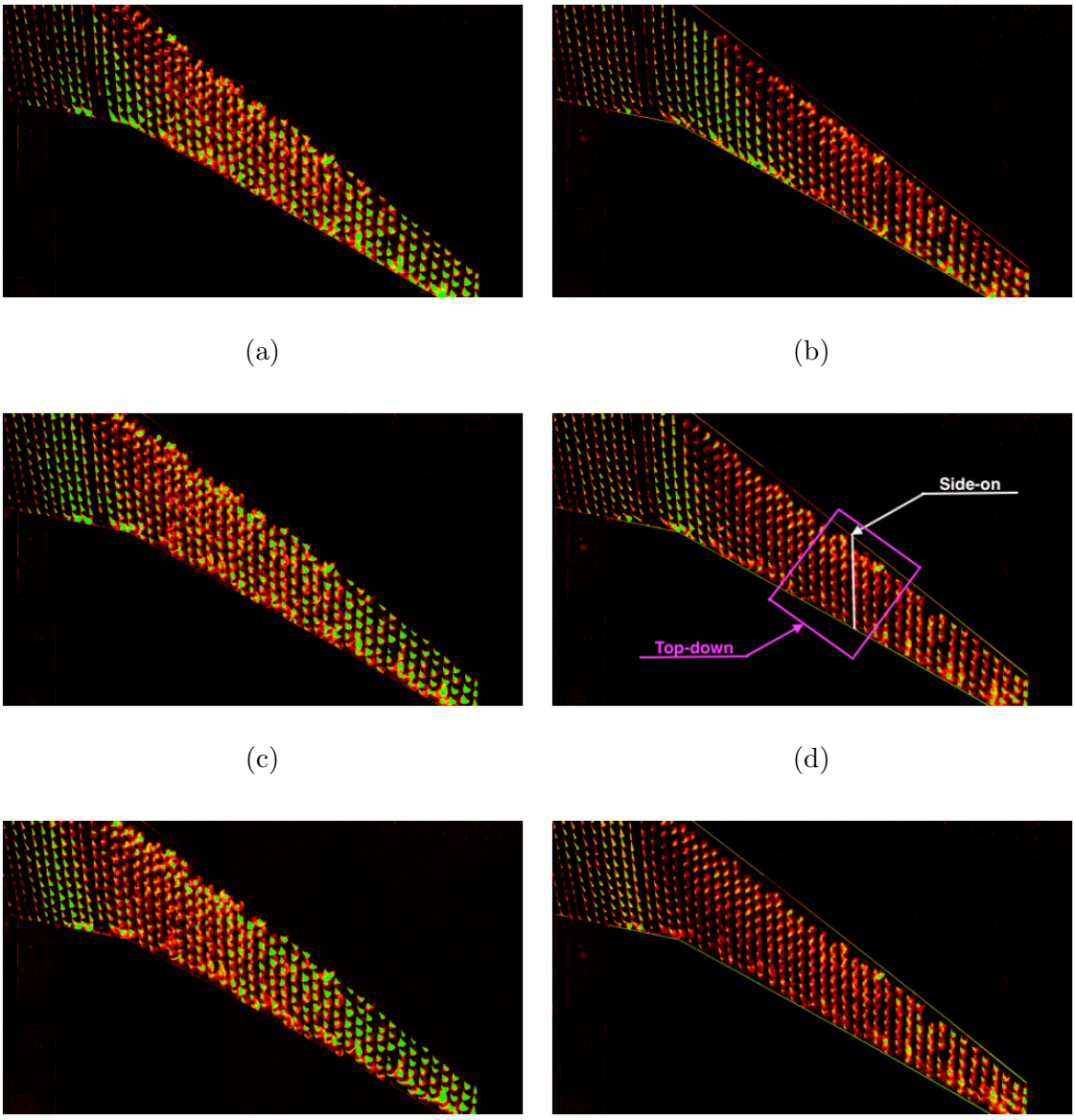

Figure 3.2: Post-processed color-coded tuft images at $\alpha = 10.5°$(3.2a, b), $\alpha = 12°$ (3.2c, d), and $\alpha = 13.5°$ (3.2e, f) during the upsweep motion, respectively for $Re_c = 0.47 \times 10^6$ (3.2a, c, e) and $Re_c = 10^6$ (3.2b, d, f). Figure 3.2d shows the PIV locations for both configurations. Free stream from the top.

the TE kink and the separation line at $\alpha = 10.5°$ and 12°. This attached region disappears at $\alpha = 13.5°$, where separation is observed over the entire wing, past the TE kink.

Reversed flow, characterized by movement at least partially upstream, is seen in the mid-span section of the wing once it is fully separated. Despite this reversed flow, the overall flow retains a strong outboard-preferred direction, particularly noticeable in the lower Re_c case. The green color tufts near the tip of the wing in Figs. 3.2a, 3.2c, and 3.2e highlights this phenomenon. Furthermore, attached flow persists in the inboard section of the wing for all Reynolds numbers at nearly all tested angles of attack, with full chord-wise separation only occurring at $\alpha = 16.5°$ for $Re_c = 0.47 \times 10^6$ and $\alpha = 18°$ for $Re_c = 10^6$ (not shown here).

The full flow visualization dataset was analyzed to identify the conditions and best region for PIV measurement. As noted above, the surface visualization appears sensitive to both angle of attack and Reynolds number in a mid-span region of the wing around 12° and $Re_c = 10^6$ as seen in Figure 3.2b, d, f. For this reason, these locations and conditions were selected for further PIV study as summarized in Table 2.4. The PIV fields of view were chosen as highlighted in Figure 3.2d. In the side-on configuration, the measurement plane is located ≈ 43 cm from the LE tip; for the top-down orientation, the frame was centered at the same location, aligned with the LE.

3.3 Statistical analysis of side-on and top-down PIV

A series of PIV datasets were acquired in two orthogonal planes and at a series of Reynolds numbers and angles of attack centered on 12°. Statistics relative to the mean flow and the three Reynolds stresses of the top-down configuration are presented as ROM reconstruction using the ELF method introduced in §2.6.

3.3.1 Side-on PIV

Figure 3.3 highlights the mean side-on flow at different angle of attacks, namely 10.5°, 12°, and 13.5°. Figure 3.4 further highlights the Reynolds normal and shear stresses $\overline{u_c'}^2$, $\overline{w_c'}^2$ and $\overline{u_c' w_c'}$. It is observed that the flow separates in the vicinity of the leading edge for all three

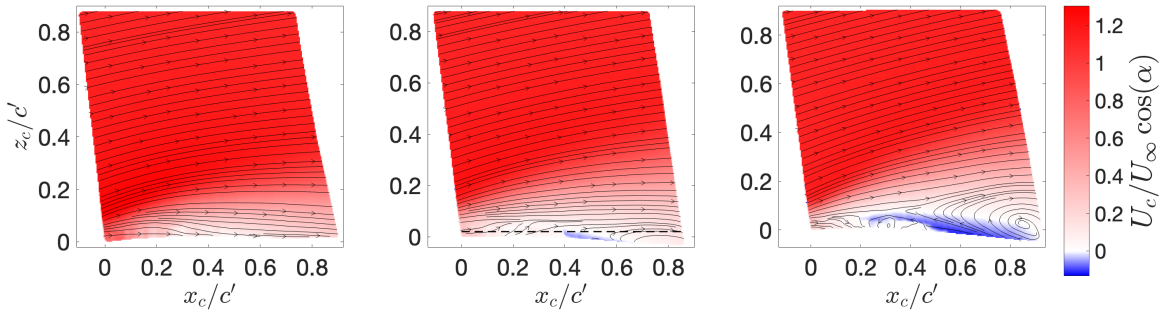

(a)

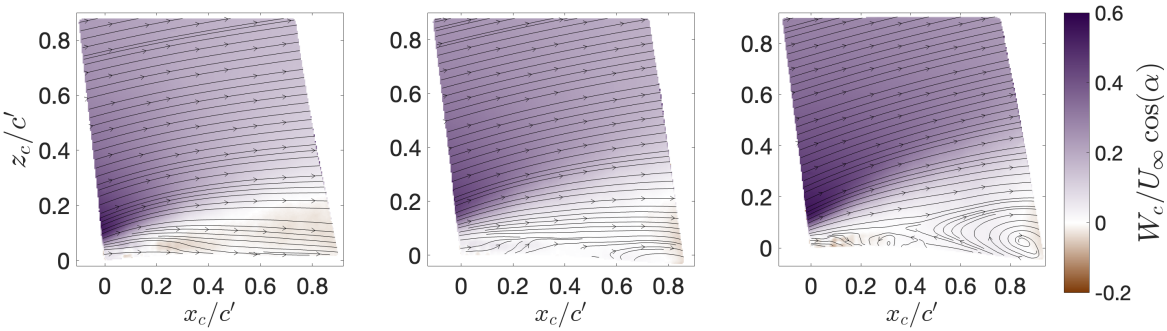

(b)

Figure 3.3: Mean streamwise (a) and vertical (b) velocity fields for the side-on configuration, at α=10.5°, α=12°, and α=13.5° respectively, for $Re_c = 10^6$. Dashed line indicates the position of the top-down PIV fame.

angles of attack and the angle of the shear layer and the extent of reversed flow increases as angle of attack increases. The first first instances of reversed flow are observed for $\alpha = 12°$ (see Figure 3.3a); this region increases for $\alpha = 13.5°$ and occupies most of the near-wall region, extending from $x_c/c' \approx 0.25$ to the trailing edge, where c' is chord length at the side-on PIV location (193 mm). Furthermore, vortical structures can clearly be noticed towards the trailing edge for the largest angle of attack. In addition, as the angle of attack increases, the region of negative vertical mean flow is seen to decrease (see Figure 3.3b).

Fig. 3.3 also shows that the width and strength of the shear layer increase at high angle of attack with higher turbulent stresses. The streamwise component $\overline{u'^2}$ (Fig. 3.4b) dominates the three stresses whether the shear and wall-normal stress are comparable in terms of magnitudes. As the angle of attack increases, the region of high $\overline{u'^2}$ component thins out and becomes more extended in the chord-wise direction and expanding in the z_c direction.

The small region of positive turbulent shear stress near the leading edge is not thought to be physical and might be due to challenging signal-to-noise issues and surface reflections in this region. The negative turbulent shear stress in the rest of the domain is consistent with turbulent production in the separated shear layer.

Similar figures exploring Reynolds number sensitivity of the separated side-on view are shown in Appendix B and follow expected trends. Differences between the moderate and highest Reynolds number were found to be minor, suggesting approximate Reynolds number independence for $Re_c > 10^6$, similar to the tufting visualizations. In addition, the shear layer thickness was found to decrease and the separation point drifts downstream with increasing Re_c, in a manner consistent with the tuft flow visualization. In addition, the amount of reversed flow in the near wall region decreases when the Reynolds number goes up, consistent with delayed flow separation produced by a more energetic boundary layer. Overall, for the tested conditions, the changes in the flow statistics due to changes in angle of attack are larger than the changes due to Reynolds number.

3.3.2 Top-down PIV

We now consider the top-down field of view to explore sensitives to Reynolds number, as well as the dominant spanwise modes and their dynamics. Figure 3.5 shows the mean quasi-streamwise and spanwise flow for the top-down configuration. For this setup, only two test points were considered, namely $\alpha = 12°$, $Re_c = 0.47 \times 10^6$, and $\alpha = 12°$, $Re_c = 10^6$. The mean flow is characterized by a dominant outwash and a broad region of reversed flow which extends from the line of attraction to the trailing edge for the lower Reynolds number case.

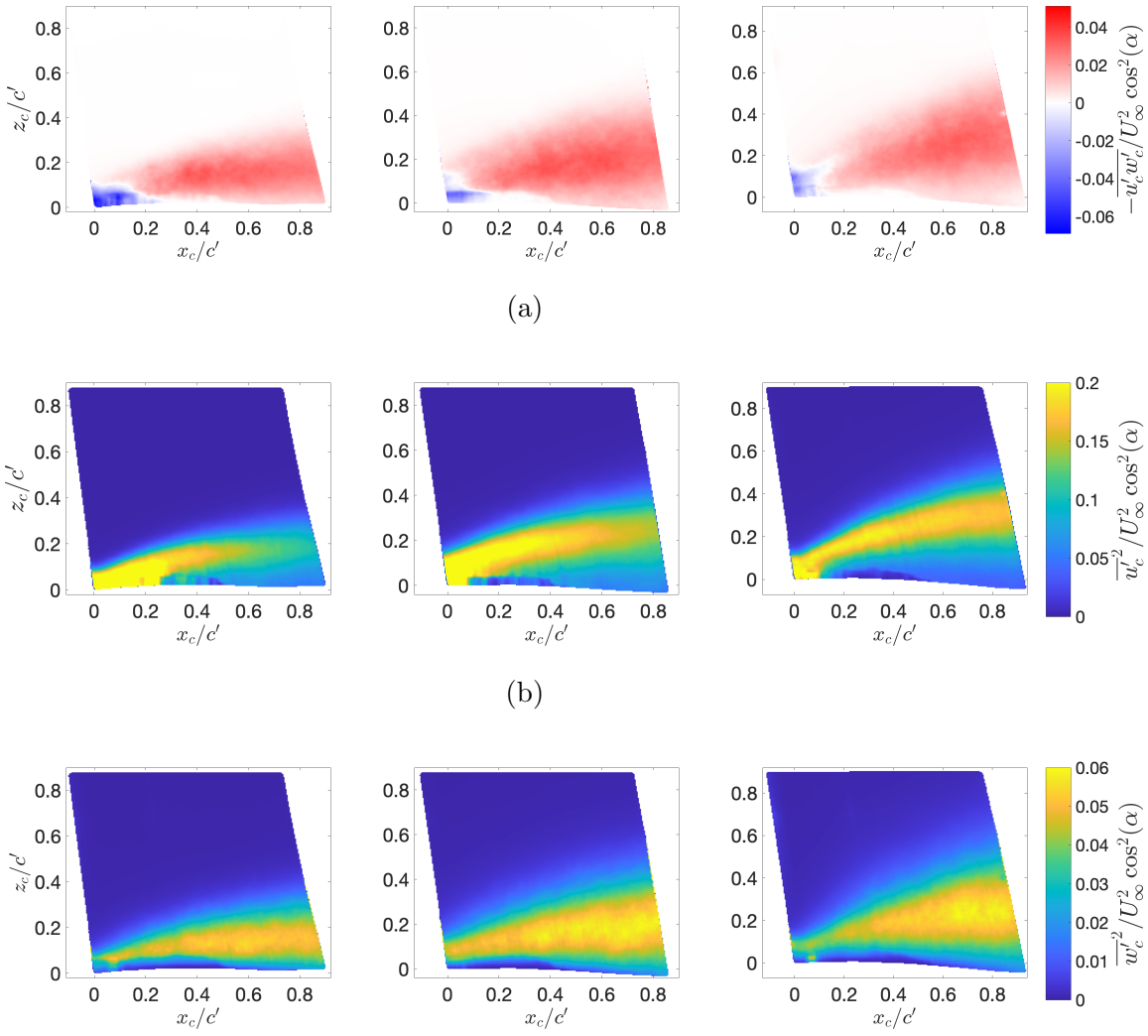

Figure 3.4: Reynolds shear stress (a), streamwise stress (b), and vertical stress (c) for the side-on configuration, at α=10.5°, α=12°, and α=13.5° respectively, for $Re_c = 10^6$.

This region reduces to $\approx 85\%$ of the chord length close to the root portion of the field of view for $Re_c = 10^6$. These observations are in accordance with the tuft visualizations discussed in §3.2, where reversed flow was observed in the mid-spar region selected for the top-down PIV configuration. Similar behavior is observed in the spanwise velocities, with slightly larger magnitudes for the higher Re_c.

Figure 3.6 show the Reynolds stresses (Reynolds decomposition aligned with these axes) for the top-down orientation at different Re_c. As the wing was in the background of this configuration, signal-to-noise and background illumination are a more significant issue, leading to spurious velocity vectors in the middle of the LE region at the higher Reynolds number and toward the trailing edge root. Despite this a number of observations can be made, and dominant modes extracted.

Both streamwise and vertical stress have their peaks along the attraction line. The magnitude of the streamwise stress is larger for $Re_c = 0.47 \times 10^6$ (relative to the freestream velocity), whereas the spanwise stress is greater for $Re_c = 10^6$ potentially due to the stronger outwash observed in Fig. 3.5. The Reynolds shear stress is predominantly negative, suggesting positive turbulent production. However there is a slight region of positive shear stress near the leading edge of the wing suggesting a similar region in the side-on view may be physical (see Fig. 3.4).

3.4 Dominant top-down POD modes

We are especially interested in the evolution and dynamics of spanwise motions within the separated region as these modes can be highly energetic and relatively slow. They may also be more sensitive indicators of dynamical shifts in the flow topology. The first five POD modes and their respective mode and cumulative energy are shown in Fig. 3.7 for an angle of attack of 12° and $Re_c = 10^6$.

We observe that the energy distribution is broadband, with only approximately 8% of the total energy in the first mode; 39 modes are needed to achieve a cumulative total of 50% of the energy. Despite this, the first five modes highlight vortical structures that appear to

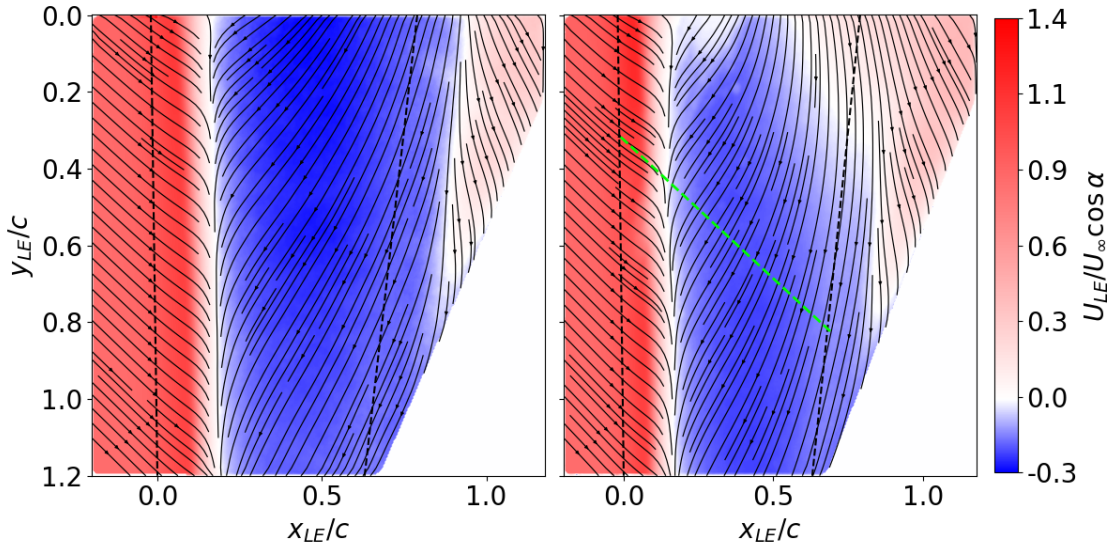

(a)

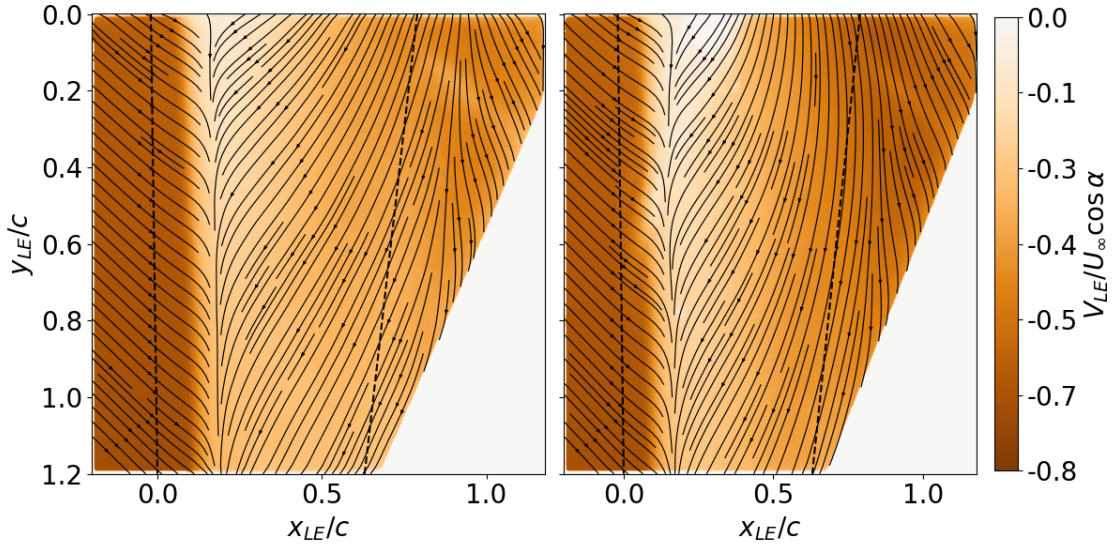

(b)

Figure 3.5: Mean quasi-streamwise (a) and spanwise (b) flow for the top-down configuration at $Re_c = 0.47 \times 10^6$ (left) and $Re_c = 10^6$ (right) respectively. The angle of attack is 12°. Flow coming from the left at ≈ -35° from the horizontal axis. Wing root is located to the top. Dashed lines indicate the leading and trailing edge respectively. Green dashed line indicates the position of the side-on PIV fame

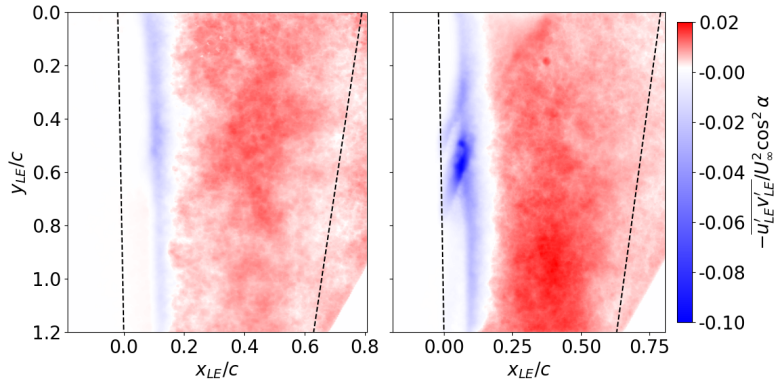

(a)

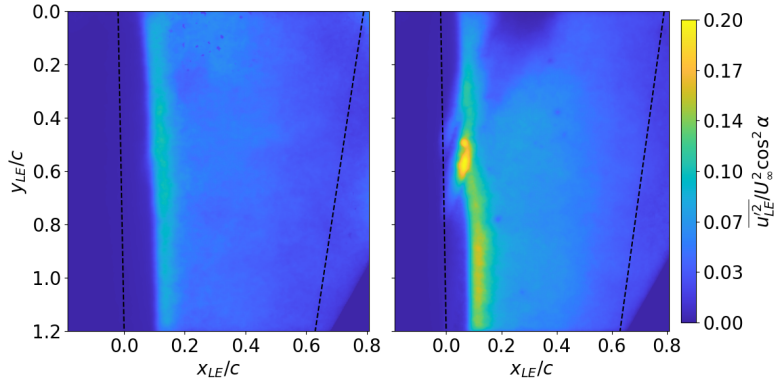

(b)

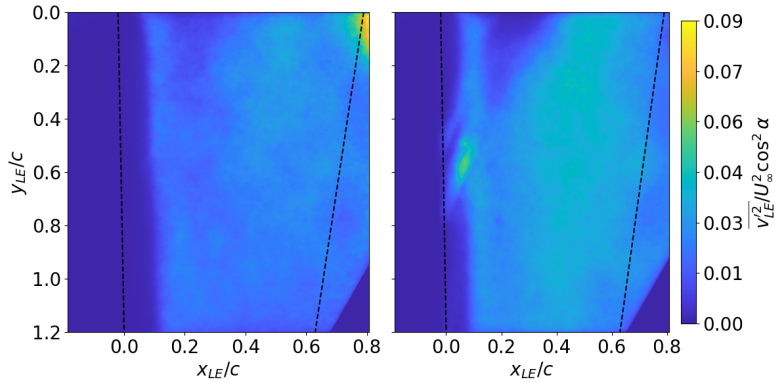

(c)

Figure 3.6: Reynolds shear stress (a), streamwise stress (b), and spanwise stress (c) for the top-down configuration at $Re_c = 0.47 \times 10^6$ and $Re_c = 10^6$ respectively (α=12°). Flow coming from the left at approximately -35° from the horizontal axis. Wing root is located to the top; dashed lines indicate the leading and trailing edge respectively.

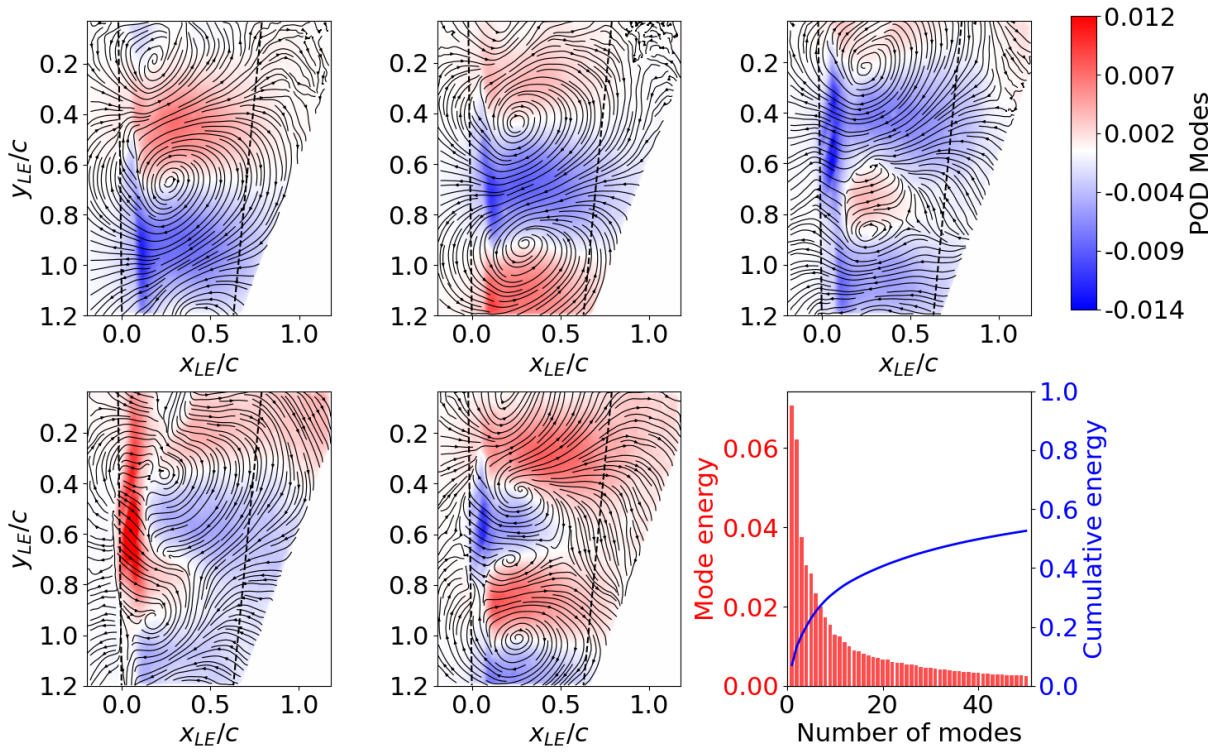

Figure 3.7: First 5 POD modes for $\alpha = 12$, $Re_c = 10^6$. The last figure (bottom right) shows the mode energy and cumulative energy for the first 60 modes.

create large-scale unsteady spanwise motions. The first two of these modes appear to be similar but shifted by half the spanwise wavelength of the structure suggesting that they are a mode pair. This is often observed when two modes interact to allow a dominant structure to convect through the domain [27]. In this case they would allow for the spanwise shifting of their dominant structure and they are thought primarily capture large-scale vortex shedding or oscillations in the boundary layer. The observed structure resembles an instantaneous stall cell, which is not revealed in the mean flow, although the spatial shape of the POD modes lacks the characteristic saddle point of the stall cell topology. The spanwise extension of this cell is about 1.7 times the mean chord length of the region of interest, which is similar to mean stall cells observed in previous experimental and numerical studies on unswept wings [12, 13, 33]. Efforts were then made to estimate the convective velocity of this structure by tracking the vortex cores in the 2-mode reconstruction frame-by-frame analysis. However, the cores translates too rapidly for the experimental setup of this test. With the laser operating at 15 Hz, successive image pairs are separated by $\approx 0.67\,\mathrm{s}$; given the 32.8cm spanwise field-of-view dimension, a vortex would have to move slower than $5\,\mathrm{m\,s^{-1}}$ to remain in the frame for two consecutive snapshots. This is much lower than the speed found by Plante et al. $V_c \approx 0.7U_\infty \tan(\Lambda) = 24.5\,\mathrm{m\,s^{-1}}$, however, the spanwise velocity observed in Fig. 3.5b is about $20\,\mathrm{m\,s^{-1}}$ in the outwash region, which is closer to numeral findings on swept wings [12]. The comparison reinforces the analogy between the dominant POD modes and stall cells and highlights how challenging it is to observe such unsteady features.

Although the present POD analysis was performed solely at a chord-based Reynolds number of $Re_c = 10^6$, results presented at High-Lift Prediction Workshop-5 (HLPW-5) indicates that the spanwise-periodic structures uncovered here are not isolated to test conditions of this study [4]. Wall-modeled large-eddy simulations for the NASA CRM-HL conducted up to $Re_c = 2 \times 10^7$ consistently show a chain of quasi-stationary separation patches whose footprints align with the "pizza-slice" wedge patterns, their persistence across more than an order of magnitude in Reynolds number suggests that the underlying global mode might persists even at higher Re than what is typical for stall cells. One of the key aspect to the

origin of "pizza-slices" is the role of the slat-bracket wakes. As angle of attack increases, bracket-induced vortices impinge on the suction surface just upstream of the separation line and may phase lock the spanwise modulation. These observations support the hypothesis that the modes extracted in the current study may persist on flight-scale wings and that their interaction with bracket wakes could be key to the formation of the characteristic pizza-slice footprint.

Mode 3, on the other hand, represents smaller-scale structures distributed across the flow domain and likely occur at higher frequencies. Modes 4 and 5 represent increasingly smaller structures with more localized flow features. While modes 3-5 do not seem to form clear mode pair, a succession of vortices are observed in the spanwise direction, centered at approximately 30% of the chord. These modes appear to extend for half the wavelength of modes 1 and 2; this is commonly seen for POD modes and is a feature of Fourier modes (harmonics). As such, the unsteady topology of the separation on this wing may be strongly non-uniform in the spanwise direction, and the separation and reattachment locations (if it exists) would may be highly variable. This progression to smaller-scale structures at higher mode numbers is consistent with a hierarchy of similar topological structures that progresses to smaller scale at higher mode number and is often observed in POD of turbulent flows. Note that we could not obtain dominant spectral peaks in the activations of these modes that were less than 7.5Hz, which is limited by the acquisition rate of the current PIV system (15Hz).

We now explore the interaction between the first three modes in an effort to explore the unsteady separation dynamics. Figure 3.8 shows co-varying scatter plots of the first three POD modal coefficients $\{a_i(t), i = 1, 2, 3\}$, color coded to show point density distribution. While the cluster of points is approximately circular when considering modes 1 and 2 (as might be expected for a mode pair), once mode 3 is considered, the scatter of activations is no longer circular. This may suggest an underlying dynamics relationship to the structure of the relationships between these modes. To further investigate this aspect, the flowfield has been reconstructed using only the first 3 modes at times when their coefficients are maximum and

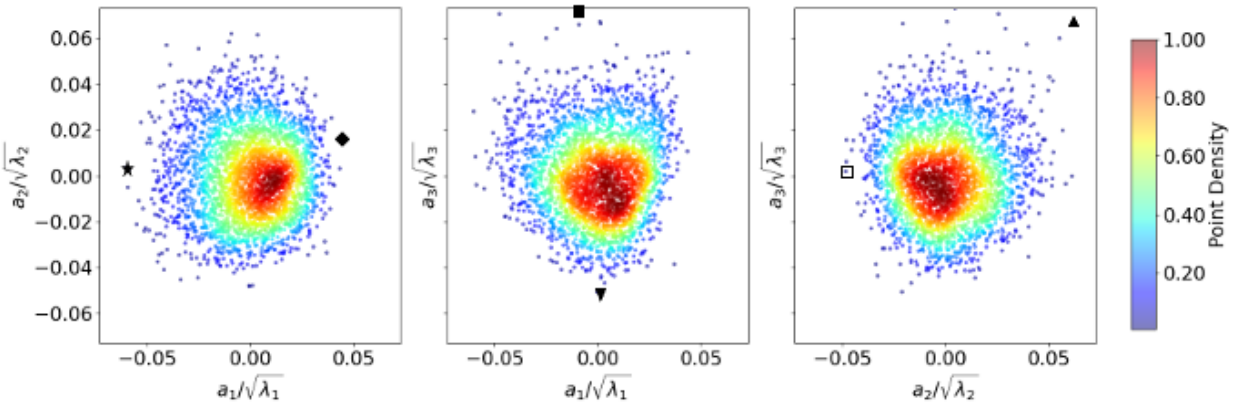

Figure 3.8: Scatter plots color coded with point density distribution of the first 3 POD coefficients. Marked the maxium and minimum values of each coefficient: a_1 max (⧫), a_1 min (★), a_2 max (▲), a_2 min (□), a_3 max (■), a_3 min (▼) respectively.

minimum, emphasizing the maximum or minimum activation of each respective mode. The reconstructed flowfield of each of these cases is shown in Fig 3.9. For each reconstruction, the mean flow has been added to the linear combination of the first three modes.

The Mode pair (1 and 2) captures large-scale spanwise periodicity and vortex dynamics across the wing. When the pair reaches its maximum value, the reconstructed flow reveals a prominent vortex structure toward the lower part of the wing, accompanied by alternating regions of upstream and downstream flow, indicative of periodic vortex shedding or oscillatory phenomena. A clear spanwise periodicity is observed, with streamlines showing oscillations across the span. On the root side, a vortex and a saddle point are visible in the reconstructions, features that are absent when the pair reaches its minimum value. At the minimum, the reconstructed flow exhibits reversed spanwise oscillations, with flow patterns shifted by half a spanwise wavelength relative to the maximum. The flow structures are consistent at both the maximum and minimum values, further reinforcing the coupling between the modes and their role as a single dynamic entity.

When Mode 3 is included, the spanwise periodicity of the mode 1 and mode 2 pairing

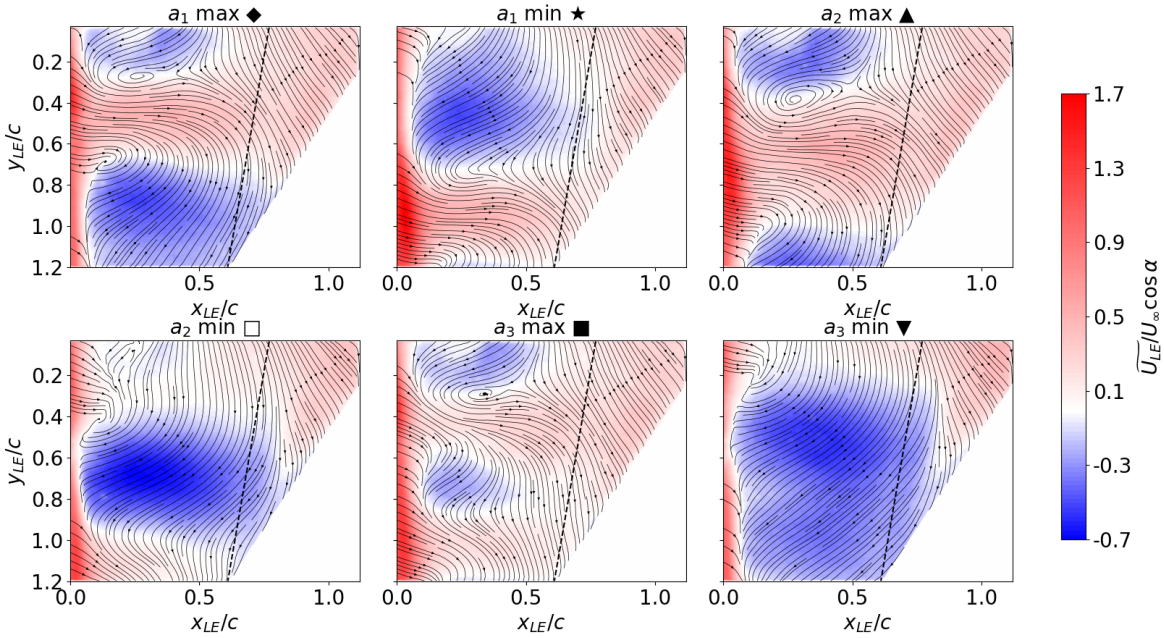

Figure 3.9: Flow reconstruction given by the mean flow and the first three POD modes when their respective POD coefficients are at a maximum or a minimum. Leading edge coincides with the vertical axis, dashed line indicates the trailing edge.

appears to be disrupted, leading to either a finer scale spanwise periodicity with shorter wavelength or a single large reversed flow region that covers almost the entire field of view. Figure 3.8 shows how when mode 3 is at its minimum, mode 1 and 2 coefficients are close to 0, suggesting that the mode 3 structure is only apparent when that representing modes 1 and 2 is dormant.

Chapter 4

CONCLUSION

This study explores the dynamic sensitivities of the separated flowfield over a 4% scale half-body high-speed CRM (CRM-HS) wing near the onset of stall. We highlight a region on the outboard section using a combination of tuft visualization and particle image velocimetry (PIV) in two orthogonal planes. The impact of changes to the flowfield on the resulting vehicle forces and moments are quantified. This study aims to explore techniques and analysis approaches (new to the Kirsten wind tunnel (KWT) at the University of Washington) that can be applied to the future study of a high-lift CRM model.

We focus on the sensitivity of the flowfield to changes in angle of attack (which is larger) and Reynolds number (which is weaker). Reynolds number insensitivity was observed for $Re_c \geq 10^6$. Pitching moment stall was achieved at $\alpha = 16.5^\circ$ for all test conditions, whereas maximum lift was not observed even at the highest angle of attack. Measurements highlighted changes to the separated structure, location and topology are likely to occur between $10^\circ \leq \alpha \leq 16^\circ$ and thus flow visualizations initially focused on a case with $\alpha = 12^\circ$ and $Re_c = 10^6$. Tuft visualizations highlighted significant changes to the extent of the separated region around this angle of attack. Separation begins at the leading edge and tip, with the separation line moving progressively toward the root as the angle of attack increases. The root region remains largely attached up to $\alpha = 16.5^\circ$ and $\alpha = 18^\circ$ respectively for $Re_c < 10^6$ and $Re_c \geq 10^6$, while the tip region exhibits separation at $\alpha = 7.5^\circ$ and $\alpha = 9^\circ$ respectively for $Re_c < 10^6$ and $Re_c \geq 10^6$. Analysis of the side-on PIV data revealed a thickening of the separated shear layer and the development of reversed flow with consequent vortical structures in the downstream region as the angle of attack increases. The shear layer angle is found to increase with the angle of attack and moves away from the wing surface. The

flow was observe to separate earlier for the lowest Reynolds number case, leading to a larger separated region. Above $Re_c = 10^6$, the flowfield exhibited approximate Reynolds number independence, in alignment with loading and tuft visualization data.

Investigation of the dominant POD modes reveals the presence of large-scale, coherent vortical structures that were not revealed in the mean flow. The first two POD modes dominate the energy spectrum and form a phase-shifted pair that captures a spanwise-periodic structure with clear symmetry. The shape of this structure resembles the size and shape of stall cells. The mode shapes and their coefficient pattern suggest a traveling wave, although the acquisition rate precludes their temporal characterization. Their robust appearance across the separated flow region and consistent anti-phase relationship support the idea that a coherent modal mechanism underlies the observed stall-like features. The third POD mode had a shorter wavelength and was found to be most active when modes one and two were not. Interaction of this mode with the mean field produced a shorter wavelength spanwise structure or a large-scale reversed flow that covered the entire field of view

From a data-processing standpoint, this study also highlights the tradeoffs between different denoising strategies. While average-subtraction and high-pass filtering proved partially effective, the POD-based background subtraction was more successful in preserving particle structures while mitigating large-area reflections. The entropy-line-fit (ELF) method proved to be an objective and reproducible tool for automatic mode thresholding in noisy environments, on the other end, it was found to suppress real flow signals, questioning the applicability of the method.

This study provides insight into the capabilities of conventional PIV systems in large-scale facilities, demonstrating a new capability for the KWT to capture unsteady flow phenomena.

REFERENCES

[1] Slotnick, J., Khodadoust, A., Alonso, J., Gropp, W., and Mavriplis, D., "CFD Vision 2030 Study: A Path to Revolutionary Computational Aerosciences," Tech. rep., 2014.

[2] Rumsey, C. L., Slotnick, J. P., and Sclafani, A. J., "Overview and summary of the third AIAA high lift prediction workshop," *Journal of Aircraft*, Vol. 56, 2019, pp. 621–644.

[3] Rumsey, C. L., Slotnick, J. P., and Woeber, C. D., "Fourth High-Lift Prediction/Third Geometry and Mesh Generation Workshops: Overview and Summary," *Journal of Aircraft*, Vol. 60, 7 2023, pp. 1160–1177.

[4] "AIAA High Lift Prediction Workshop," 2025.

[5] Taira, K., Brunton, S. L., Dawson, S. T., Rowley, C. W., Colonius, T., McKeon, B. J., Schmidt, O. T., Gordeyev, S., Theofilis, V., and Ukeiley, L. S., "Modal analysis of fluid flows: An overview," *AIAA Journal*, Vol. 55, 2017, pp. 4013–4041.

[6] Clark, A. M., Slotnick, J. P., Taylor, N., and Rumsey, C. L., "Requirements and challenges for cfd validation within the high-lift common research model ecosystem," *AIAA AVIATION 2020 FORUM*, Vol. 1 PartF, American Institute of Aeronautics and Astronautics Inc, AIAA, 2020.

[7] Barlow, J. B., Rae, W. H., and Pope, A., *Low-speed wind tunnel testing*, Wiley, 1999.

[8] Sandham, N. D., "Transitional separation bubbles and unsteady aspects of aerofoil stall," *Aeronautical Journal*, Vol. 112, Royal Aeronautical Society, 2008, pp. 395–404.

[9] AlMutairi, J., ElJack, E., and AlQadi, I., "Dynamics of laminar separation bubble over NACA-0012 airfoil near stall conditions," *Aerospace Science and Technology*, Vol. 68, 9 2017, pp. 193–203.

[10] Eaton, J. K. and Johnston, J. P., *Low Frequency Unsteadyness of a Reattaching Turbulent Shear Layer*, Springer Berlin Heidelberg, 1982, pp. 162–170.

[11] Rodríguez, D. and Theofilis, V., "On the birth of stall cells on airfoils," *Theoretical and Computational Fluid Dynamics*, Vol. 25, 2011, pp. 105–117.

[12] Plante, F., Dandois, J., Beneddine, S., Éric Laurendeau, and Sipp, D., "Link between subsonic stall and transonic buffet on swept and unswept wings: From global stability analysis to nonlinear dynamics," *Journal of Fluid Mechanics*, Vol. 908, Cambridge University Press, 2020.

[13] Manni, L., Nishino, T., and Delafin, P. L., "Numerical study of airfoil stall cells using a very wide computational domain," *Computers and Fluids*, Vol. 140, 11 2016, pp. 260–269.

[14] Dell'Orso, H. and Amitay, M., "Parametric investigation of stall cell formation on a NACA 0015 airfoil," *AIAA Journal*, Vol. 56, 2018, pp. 3216–3228, Citation 32.

[15] Williams, O., Samuell, M., Sarwas, S., Robbins, M., Ferrante, A., and Boeing, W. E., "Experimental study of a CFD validation test case for turbulent separated flows," *AIAA SciTech 2020 Forum*, 2020.

[16] Manohar, K. H., Williams, O., Martinuzzi, R. J., and Morton, C., "Temporal super-resolution using smart sensors for turbulent separated flows," *Experiments in Fluids*, Vol. 64, 5 2023.

[17] Vassberg, J. C., DeHaan, M. A., Rivers, S. M., and Wahls, R. A., "Development of a common research model for applied CFD validation studies," *Collection of Technical Papers - AIAA Applied Aerodynamics Conference*, American Institute of Aeronautics and Astronautics Inc., 2008.

[18] Tunnel, K. W., "KWT Technical guide," 2022.

[19] Eder, S., Hufnagel, K., and Tropea, C., "Semi-span testing in wind tunnels," *25TH INTERNATIONAL CONGRESS OF THE AERONAUTICAL SCIENCES*, 2006.

[20] Voogt, F. D. and Ganapathisubramani, B., "Effects of a trailing-edge flap on stall cell characteristics of a NACA0012 wing," *Flow*, Vol. 2, 7 2022.

[21] Willert, C. E. and Gharib, M., "Experiments in Fluids Digital particle image velocimetry," Tech. rep., 1991.

[22] Keane, R. D. and Adrian, R. J., "Theory of cross-correlation analysis of PIV images," Tech. rep., 1992.

[23] Adrian, R. and Westerweel, J., *Particle Image Velocimetry*, Cambridge Aerospace Series, Cambridge University Press, 2011.

[24] Raffel, M., Willert, C. E., Scarano, F., Kähler, C. J., Wereley, S. T., and Kompenhans, J., *Particle Image Velocimetry: A Practical Guide*, Springer International Publishing, 2018.

[25] Westerweel, J. and Scarano, F., "Universal outlier detection for PIV data," *Experiments in Fluids*, Vol. 39, 12 2005, pp. 1096–1100.

[26] Brunton, S. L. and Kutz, N. J., *Data-Driven Science and Engineering*, 2019.

[27] Lumley, J. L., "The Structure of Inhomogeneous Turbulent Flows," *Atmospheric Turbulence and Radio Wave Propagation*, edited by A. M. Yaglom and V. I. Tatarski, Nauka, Moscow, Russia, 1967, pp. 166–178.

[28] Berkooz, G., Holmes, P., and Lumley, J. L., "The Proper Orthogonal Decomposition in the Analysis of Turbulent Flows," *Annual Review of Fluid Mechanics*, Vol. 25, 1 1993, pp. 539–575.

[29] Mendez, M. A., Raiola, M., Masullo, A., Discetti, S., Ianiro, A., Theunissen, R., and Buchlin, J. M., "POD-based background removal for particle image velocimetry," *Experimental Thermal and Fluid Science*, Vol. 80, 1 2017, pp. 181–192.

[30] Brindise, M. C. and Vlachos, P. P., "Proper orthogonal decomposition truncation method for data denoising and order reduction," *Experiments in Fluids*, Vol. 58, 4 2017.

[31] Aubry, N., gis Guyonnet, R., and Lima, R., "Spatiotemporal Analysis of Complex Signals: Theory and Applications," Tech. rep., 1991.

[32] Bulusu, K. V. and Plesniak, M. W., "Shannon entropy-based wavelet transform method for autonomous coherent structure identification in fluid flow field data," *Entropy*, Vol. 17, 2015, pp. 6617–6642.

[33] Yon, S. A. and Katz, J., "Study of the unsteady flow features on a stalled wing," *AIAA Journal*, Vol. 36, 1998, pp. 305–312.

Appendix A

TUFT VISUALIZATION COMPLEMENT

In the following, color-coded tuft visualization images are shown for the nominal case ($Re_c = 10^6$). Both picth up and pitch down data are presented for angle between 6° and 18°.

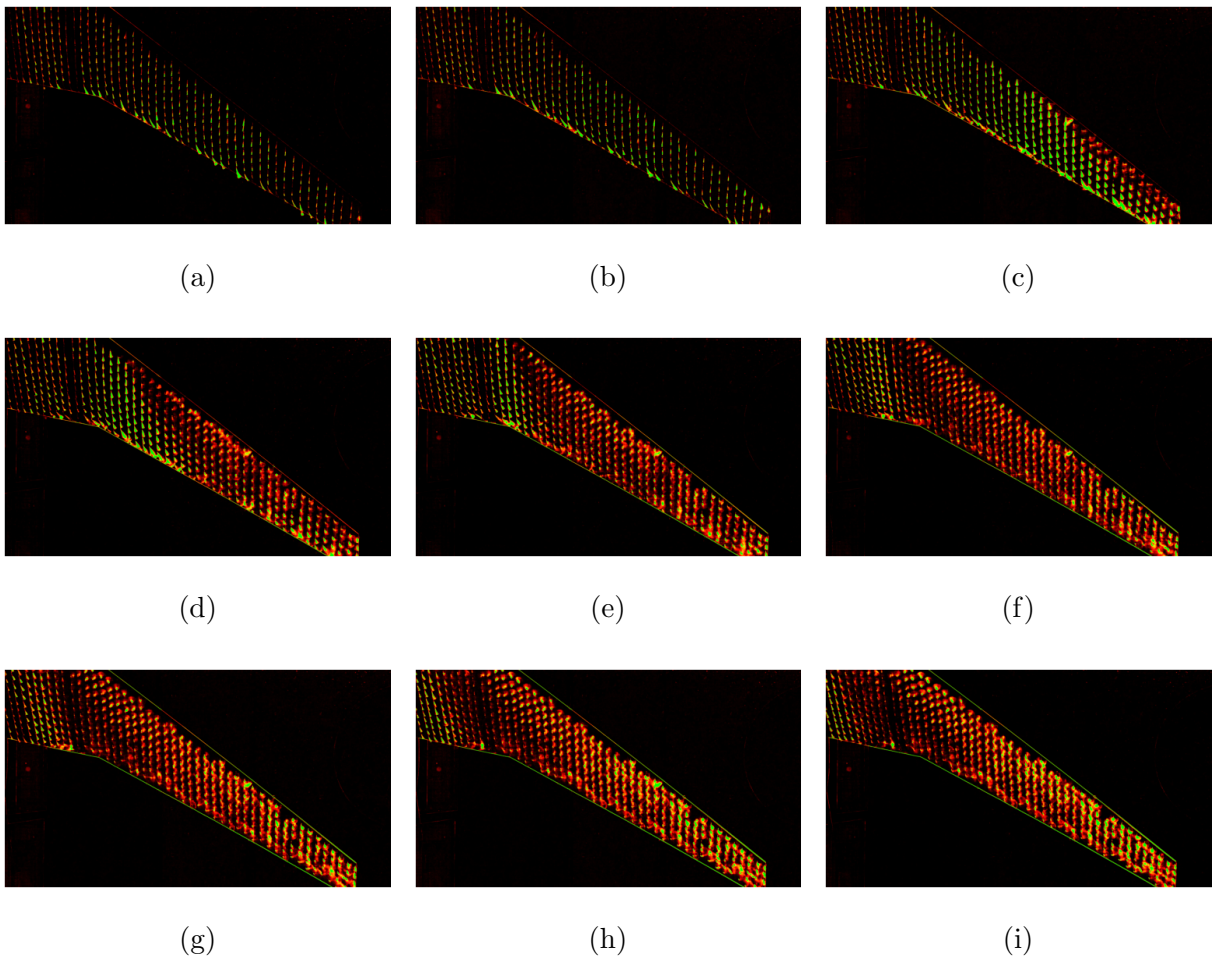

(a) (b) (c)

(d) (e) (f)

(g) (h) (i)

Figure A.1: Post-processed color-coded tuft images from 6° to 18° at 1.5° increment for the pitch up motion.

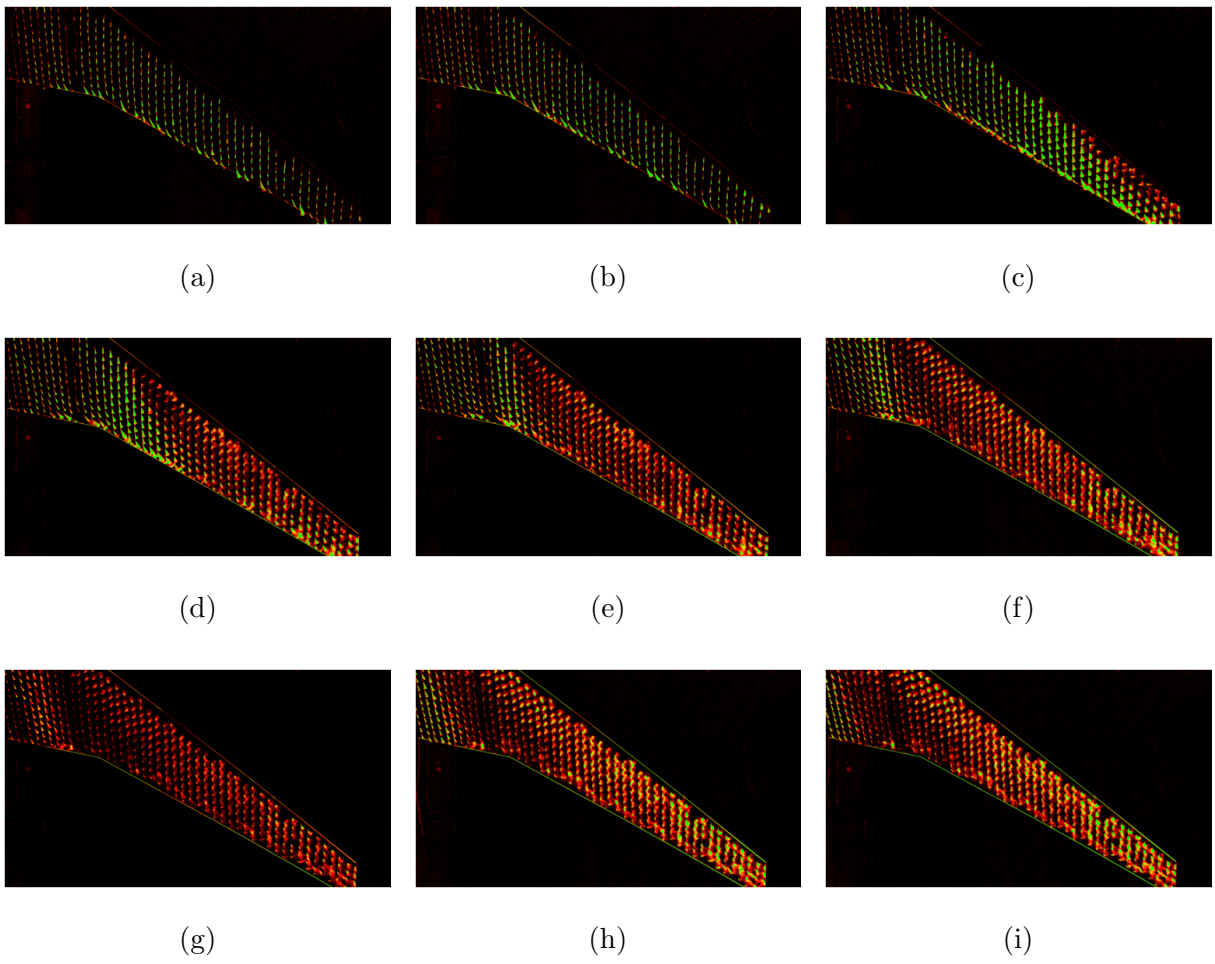

Figure A.2: Post-processed color-coded tuft images from 6° to 18° at 1.5° increment for the pitch down motion.

Appendix B

SIDE-ON PIV AT DIFFERENT REYNOLDS NUMBERS

In the following, the comparison of mean flow and flow statistics for the nominal condition at different Reynolds numbers is shown.

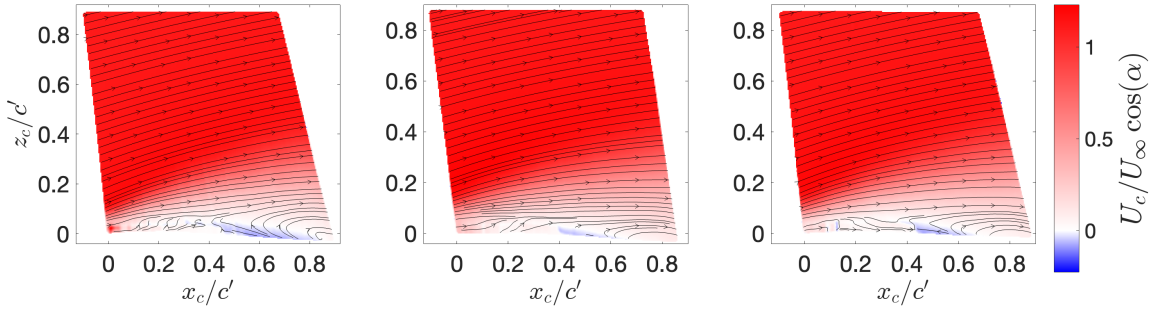

(a)

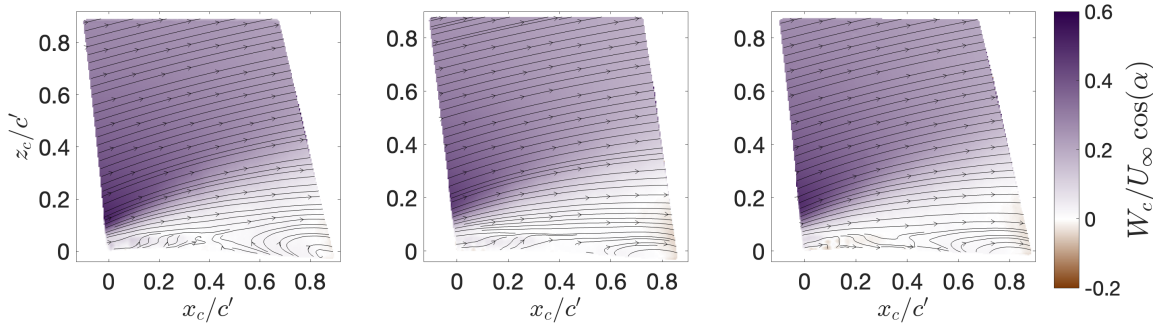

(b)

Figure B.1: Mean streamwise (a) and vertical (b) velocity fields for the side-on configuration, at $Re_c = 0.47 \times 10^6$, $Re_c = 10^6$, and $Re_c = 1.48 \times 10^6$ respectively, for α=12°.

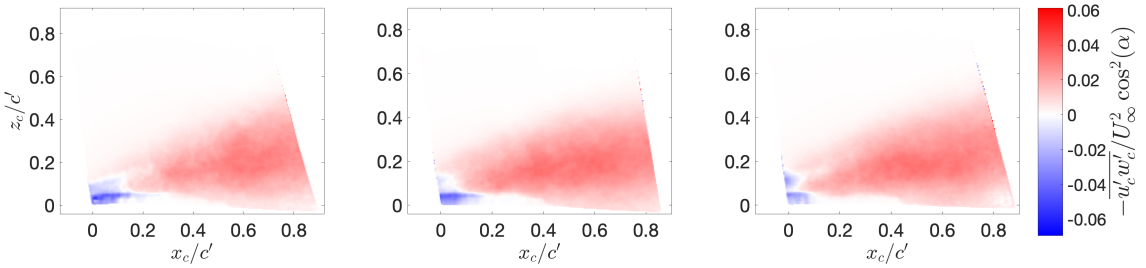

(a)

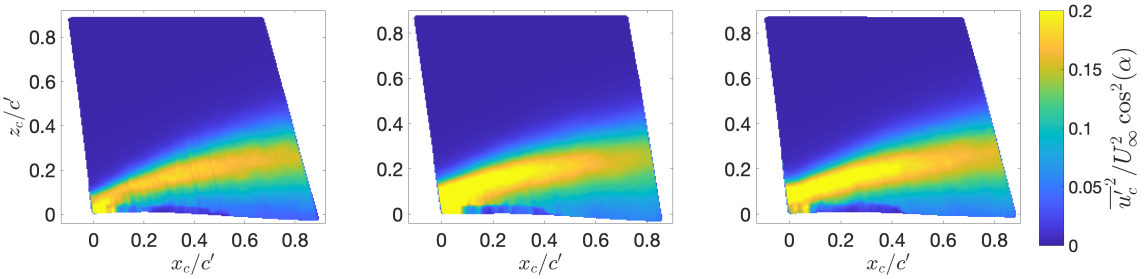

(b)

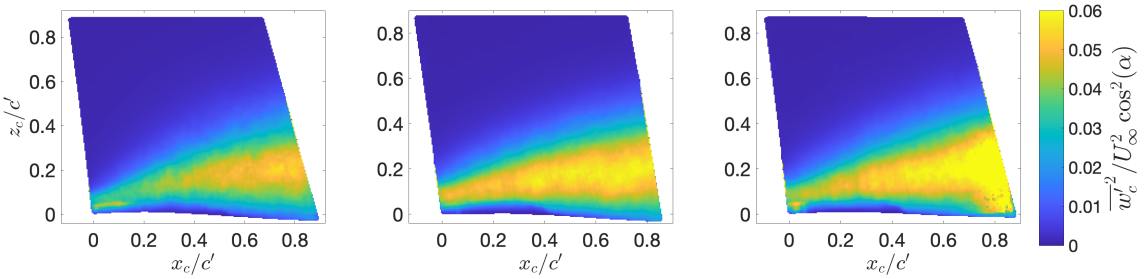

(c)

Figure B.2: Reynolds shear stress (a), streamwise stress (b), and vertical stress (c) for the side-on configuration, at $Re_c = 0.47 \times 10^6$, $Re_c = 10^6$, and $Re_c = 1.48 \times 10^6$ respectively, for α=12°.